In contrast to clinical manifestations that are consistent with idiopathic PD, the brains of patients with *LRRK2* mutations exhibit more diverse pathological alterations. In addition to the classical nigral degeneration predominantly with LB pathology found in the brains of patients with idiopathic PD and dementia with LBs (DLB) (8, 12–15), tau-positive inclusions reminiscent of tauopathies (15, 16), ubiquitin-positive pathology only (17), or the distinct absence of pathological inclusions (12, 18) are less commonly observed. These findings suggest that LRRK2 may be central to or upstream of pathogenic pathways that regulate α-synuclein or tau protein deposition and that disruptions of this pathway caused by *LRRK2* mutations precipitate a PD phenotype. To address this notion, several research groups have investigated the distribution of LRRK2 protein in normal and pathological human brains to determine whether it is localized to LBs or neurofibrillary tangles (NFTs) in synucleinopathies or tauopathies, respectively. The LRRK2 protein has been identified in various brain regions including the striatum, cerebral cortex, hippocampus, and cerebellum but at markedly lower levels in the substantia nigra (19–23). Nevertheless, LRRK2 protein is localized to a subset of α-synuclein–positive LBs in the substantia nigra pars compacta of PD and DLB brains (19, 24–27). Furthermore, a previous report showed that diverse tau-positive inclusions in the brains of patients with AD, parkinsonism dementia complex of Guam and Pick disease (PiD), and intraneuronal inclusions in the spinal cords of patients with amyotrophic lateral sclerosis were immunopositive for LRRK2, suggesting that it may also be localized to tau-positive inclusions in tauopathies and possibly ubiquitin-positive inclusions in TDP-43 proteinopathies (28). In contrast, others have reported that LRRK2 is not localized to NFTs (25). Thus, consistent results regarding the localization of LRRK2 protein in neurodegenerative disorders have not yet been obtained.

In the present study, we investigated a variety of neurodegenerative disorders and found that LRRK2 is localized to a subset of α-synuclein–positive brainstem-type LBs but not to α-synuclein–positive cortical-type LBs, tau-positive NFTs, or other tau inclusions, nor to TDP-43–positive inclusions. In addition, we often observed LRRK2-positive enlarged granules or vacuoles within neurons of the substantia nigra pars compacta and limbic area of pathological brains (particularly in PD and DLB brains) that are obviously distinct from the smaller LRRK2-positive punctate structures normally present in neurons of control brains. These pathological LRRK2-positive enlarged structures frequently colocalized with the late-endosomal marker, Rab7B, and occasionally with the lysosomal marker, lysosomal-associated membrane protein 2 (LAMP-2). These results suggest a role for LRRK2 in the endosomal-lysosomal system in the pathogenesis of LB diseases.

MATERIALS AND METHODS

Case Material

We examined 21 postmortem brains from patients with neurodegenerative disorders, including PD, DLB, AD, PiD, progressive supranuclear palsy, corticobasal degeneration, and frontotemporal lobar degeneration with ubiquitin inclusions (FTLD-U). The patients had no family history of neurological or psychiatric disorders. Clinical and demographic data are given in Table 1. The PD cases fulfilled the diagnostic criteria for PD (29), DLB cases fulfilled the consensus criteria for a high likelihood of DLB (30), and AD cases fulfilled consensus criteria for a high likelihood of AD (31). The neuropathologic features of each case of PD, DLB, and AD were assessed as previously described (32) (Table 2). In addition, 7 normal elderly control cases with no history of neurological disorders or no evidence of significant neuropathologic abnormalities were also studied (Table 1).

Antibodies

Rabbit polyclonal anti-LRRK2 antibodies were generated using keyhole limpet hemocyanin–coupled synthetic peptides corresponding to human LRRK2 amino acids 334 to 347 (JH5517) and 2500 to 2515 (JH5514), as previously described (35, 36). A commercial rabbit polyclonal anti-LRRK2 antibody, NB300-267, was also used (human LRRK2, amino acids 920–945, Novus Biologicals, Littleton, CO; [37]). These 3 anti-LRRK2 antibodies have previously been shown to recognize a protein band of approximately 280 kd, corresponding to the predicted size of LRRK2 protein by Western blot analysis of cell or tissue lysates and have been used in previous studies for immunohistochemistry (12, 19, 26–28, 35–38). Additional antibodies used were anti–phosphorylated α-synuclein (pSer129 [39]), anti-amyloid β, anti–paired helical filament (PHF) tau, anti-TAR-DNA–binding protein 43 (TDP-43), anti–LAMP-2, anti-Rab7B, anti–cytochrome oxidase *c* subunit IV (COX IV), and anti–trans-Golgi network protein 2 (TGOLN2 , also known as TGN38) (Table 3).

Immunohistochemical and Immunofluorescent Analysis

Cerebral hemispheres and brainstem, including the midbrain, pons and medulla oblongata, amygdala, hippocampus, entorhinal cortex, and inferior temporal cortex (Brodmann

TABLE 1. Clinical and Demographic Data

Group	n (Male-Female)	Age, Years	Brain Weight, g	Disease Duration, Years
PD	2 (1:1)	58 ± 19.8	1,190 ± 156	7 ± 1.4
DLB	6 (4:2)	69.3 ± 10.6	1,071 ± 137	4.8 ± 1.3
AD	6 (3:3)	77.3 ± 11	1,080 ± 124	7 ± 3.7
PiD	2 (1:1)	72.5 ± 2.1	790 ± 156	10.5 ± 6.4
PSP	1 (1:0)	67	1,160	5
CBD	1 (0:1)	72	867	16
FTLD-U	3 (2:1)	67.3 ± 3.1	1,008 ± 172	8.7 ± 3.8
Control	7 (4:3)	73.9 ± 5.2	1,294 ± 34	—

Ages, brain weights, and disease durations for each group are presented as mean ± SD.
Control, aged normal subjects.
AD, Alzheimer disease; CBD, corticobasal degeneration; DLB, dementia with Lewy bodies; FTLD-U, frontotemporal lobar degeneration with ubiquitin-positive inclusions; PD, Parkinson disease; PiD, Pick disease; PSP, progressive supranuclear palsy.

TABLE 2. Neuropathologic Data on Parkinson Disease, Dementia With Lewy Bodies, and Alzheimer Disease Cases

Case No.	Aβ Stage	NF Stage	Lewy Stage	AD Criteria	DLB Criteria
PD1	B	I	I>	NA	NA
PD2	A	I	I>	NA	NA
DLB1	C	IV	IV	NA	High (diffuse neocortical)
DLB2	C	II	III	NA	High (diffuse neocortical)
DLB3	0	II	IV	NA	High (diffuse neocortical)
DLB4	C	II	III	NA	High (diffuse neocortical)
DLB5	C	II	III	NA	High (diffuse neocortical)
DLB6	C	II	III	NA	High (diffuse neocortical)
AD1	C	V	NA	High	NA
AD2	C	V	NA	High	NA
AD3	C	IV	NA	High	NA
AD4	C	V	NA	High	NA
AD5	C	V	NA	High	NA
AD6	C	V	NA	High	NA

Amyloid β (Aβ) Stages (A–C) and neurofibrillary (NF) Stages (I–VI) were determined according to Braak staging (33). Lewy stages (I–IV) in dementia with Lewy bodies (DLB) were assigned according to our previous protocol (34). Consensus criteria were used to diagnose Parkinson disease (PD) (29), DLB (30), and AD (31).

NA, not applicable.

Area 20), of all brains were fixed in 4% paraformaldehyde in 0.1 mol/L phosphate buffer, pH 7.4 (PBS), embedded in paraffin, and cut into 6-μm-thick sections. After removal of the paraffin, endogenous peroxidase activity was quenched for 30 minutes with 1.5% H_2O_2 in methanol. After rehydration, antigens were retrieved with autoclaving or treatment with 70% formic acid. Sections were blocked for 1 hour with 10% normal goat or horse serum and then incubated overnight at 4°C with primary antibodies at the appropriate dilution (Table 3). Sections were incubated for 1 hour with biotinylated secondary antibody, either goat anti-rabbit or horse anti-mouse IgG (1:500, Vector Laboratories, Burlingame, CA), and processed for 45 minutes with avidin-biotin horseradish peroxidase complex (ABC) (Vector Laboratories). Immunoreactivity was visualized with 0.5 mg/mL 3,3,-diaminobenzidine tetrachloride and 0.03% H_2O_2. Washes (2 for 20 minutes each) in PBS were carried out between each step. The sections were lightly counterstained with hematoxylin, dehydrated through graded alcohols, cleared with xylene, and mounted in mounting medium. Some sections were also double immunostained with antibodies to LRRK2 and phosphorylated α-synuclein, PHF tau, LAMP-2, Rab7B, COX IV, or TGOLN2. Immunoreactivity was detected using the ABC–horseradish peroxidase and the ABC–alkaline phosphatase methods (ABC-alkaline phosphatase kit) (Vector Laboratories) and visualized with 3,3,-diaminobenzidine tetrachloride and fast blue, respectively. The sections were coverslipped with 90% glycerol in PBS.

For double labeling immunofluorescence, the primary antibodies were used at lower dilutions. After incubation overnight at 4°C in antibody to LRRK2 (JH5514, JH5517, or NB300-267; 1:200 dilution) together with antibody to PHF tau, LAMP-2, Rab7B, COX IV, or TGOLN2, the sections were incubated for 3 hours with AlexaFluor-488 goat anti-rabbit IgG for antibody to LRRK2 and AlexaFluor-594 goat anti-mouse IgG for antibody to PHF tau, LAMP-2, Rab7B, COX IV, or TGOLN2 (Molecular Probes, Carlsbad, CA). Immunofluorescence was visualized on an Olympus Fluoview FV1000 Confocal Microscope.

Morphometric Analysis

For the quantification of the LRRK2-immunoreactive area per cell in 6 DLB, 6 AD, and 7 aged control cases, immunohistochemistry was carried out under identical experimental conditions that resulted in comparable background staining intensities among all cases. For each brain, 25 neurons with the nucleolus in focus on the section were selected at random from several fields throughout the entorhinal cortex. Evaluation of LRRK2-immunoreactive areas for each neuron was performed with the Win Roof version 5 (Mitani Corp, Japan) at 1,000× magnification interfaced with an Olympus digital CCD camera (DP71) mounted on an Olympus BX51

TABLE 3. Antibodies

Antibody	Type, Species	Source and Reference	Staining Dilution
Anti-LRRK2 (JH5514)	Polyclonal, rabbit	In-house (Johns Hopkins)	1:400
Anti-LRRK2 (JH5517)	Polyclonal, rabbit	In-house (Johns Hopkins)	1:400
Anti-LRRK2 (NB300-267)	Polyclonal, rabbit	Novus Biologicals, Littleton, CO (37)	1:400
Anti–phosphorylated α-synuclein (Pser129)	Monoclonal, mouse	Gift from Dr. T. Iwatsubo, University of Tokyo, Tokyo, Japan (39)	1:20,000
Anti–amyloid-β	Polyclonal rabbit	Gift from Dr. T. Ishii (Sagamidai Hospital, Kanagawa, Japan)	1:5000
Anti–PHF tau (AT8)	Monoclonal, mouse	Innogenetics, Zwijnaarde, Belgium	1:2000
Anti–TDP-43 (10782-1-AP)	Polyclonal, rabbit	ProteinTech Group, Chicago, IL	1:2000
Anti–LAMP-2 (H4B4)	Monoclonal, mouse	Santa Cruz Biotechnology, Santa Cruz, CA	1:200
Anti-Rab7B (3B3)	Monoclonal, mouse	Abnova Corporation, Taipei, Taiwan	1:200
Anti–COX IV	Monoclonal, mouse	Abcam, Tokyo, Japan	1:400
Anti-TGN38/TGOLN2 (M02)	Monoclonal, mouse	Abnova Corporation, Taipei, Taiwan	1:200

COX IV, cytochrome oxidase *c* subunit IV; LAMP-2, lysosomal-associated membrane protein 2; PHF, paired helical filament; TDP-43, TAR-DNA binding protein 43; TGOLN2, trans-Golgi network protein 2.

microscope. The LRRK2-positive enlarged structures were selected as green immunoreactive dots using 2-color extraction in the Win Roof program. The areas were then measured. The total cytoplasmic area occupied by faint brown immunoreactivity was also selected as a green cytoplasmic area using 2-color extraction with similar threshold values in each section followed by the optical dissection of the nucleus if needed, and then the area was quantified. Differences in mean volume of LRRK2-positive enlarged structures among the 3 groups of brains were analyzed by 2-tailed unpaired Student *t*-test; values of $p < 0.05$ were considered significant. Measurements of the diameter of LRRK2-positive enlarged structures in the digital images were carried out using the measurement program of line length of the Win Roof software.

Cell Counting

The numbers of neurons with or without enlarged structures, in which LRRK2 immunoreactivity colocalized to Rab7B immunoreactivity, were counted using microscopic fields at 400× magnification (field size, 0.025 mm^2) in the basal amygdaloid nucleus of DLB brains. The average numbers of neurons in 3 fields were calculated in each DLB case for determining the proportions of neurons with double-positive enlarged structures.

RESULTS

LRRK2 Localizes to Brainstem-Type LBs but Not to Tau- or TDP-43–Positive Pathological Inclusions

We previously reported that a small subset of brainstem-type LBs in the substantia nigra pars compacta in 2 PD cases were immunoreactive for LRRK2 using 2 distinct anti-LRRK2 antibodies (19). Here, we investigated the localization of LRRK2 in the brainstem of 2 PD and 6 DLB cases using 3 anti-LRRK2 antibodies that were raised against distinct LRRK2 peptide sequences (Fig. 1A). LRRK2 immunoreactivity was observed in a small subset of brainstem-type LBs in the substantia nigra pars compacta, locus coeruleus and dorsal vagal nucleus of PD and DLB brains (Figs. 1B–G). The immunoreactivity was predominantly localized to the core (Figs. 1B, D, E, G) or to the rim surrounding the core (Figs. 1C, F) of the LBs; the LB halos were usually LRRK2-immunonegative. The LRRK2 immunopositivity in these LBs colocalized with phosphorylated α-synuclein (Figs. 1H, I), although the latter was predominant in the halos. Counts in consecutive sections immunostained with 1 of these antibodies indicated that approximately 15% to 40% of phosphorylated α-synuclein-positive brainstem-type LBs are also immunopositive for LRRK2.

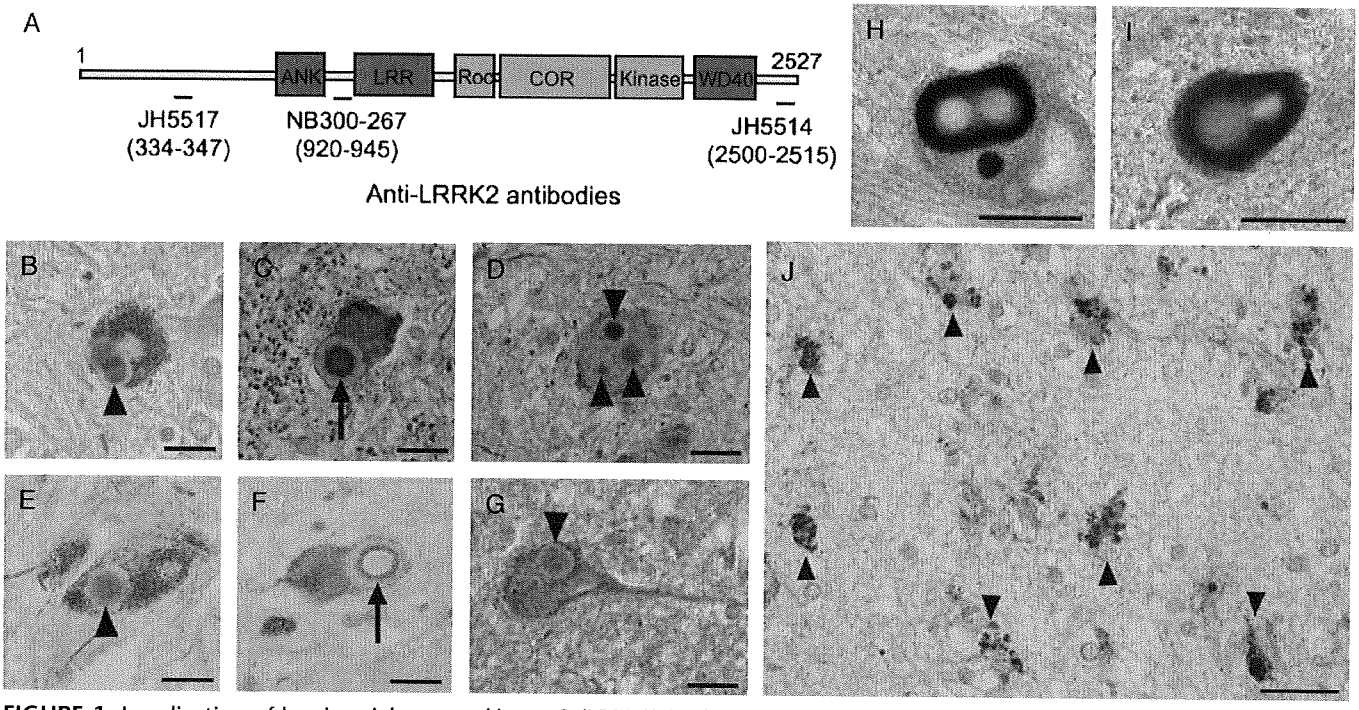

FIGURE 1. Localization of leucine-rich repeat kinase 2 (LRRK2) in the brains of Parkinson disease (PD) and dementia with Lewy bodies (DLB) cases. **(A)** The location of peptides recognized by 3 LRRK2-specific polyclonal antibodies are shown aligned to the protein domain structure of LRRK2. **(B–G)** The immunoreactivity of LRRK2 in the core (arrowheads) and its outer rim (arrows) of brainstem-type LBs in the substantia nigra pars compacta (**B, E**), locus caeruleus (**C, D, G**), or dorsal vagal nucleus (**F**) of PD (**B, C, E, F**) or DLB (**D, G**) brains. **(H, I)** Double immunolabeling for LRRK2 (brown) and phosphorylated α-synuclein (blue) shows colocalization of LRRK2 with α-synuclein–positive brainstem-type LBs (dark brown). **(J)** The immunohistochemistry of LRRK2 in the amygdala of a DLB brain; LRRK2-positive enlarged granules are observed within the cytoplasm of neurons (arrowheads). Scale bar = 20 μm.

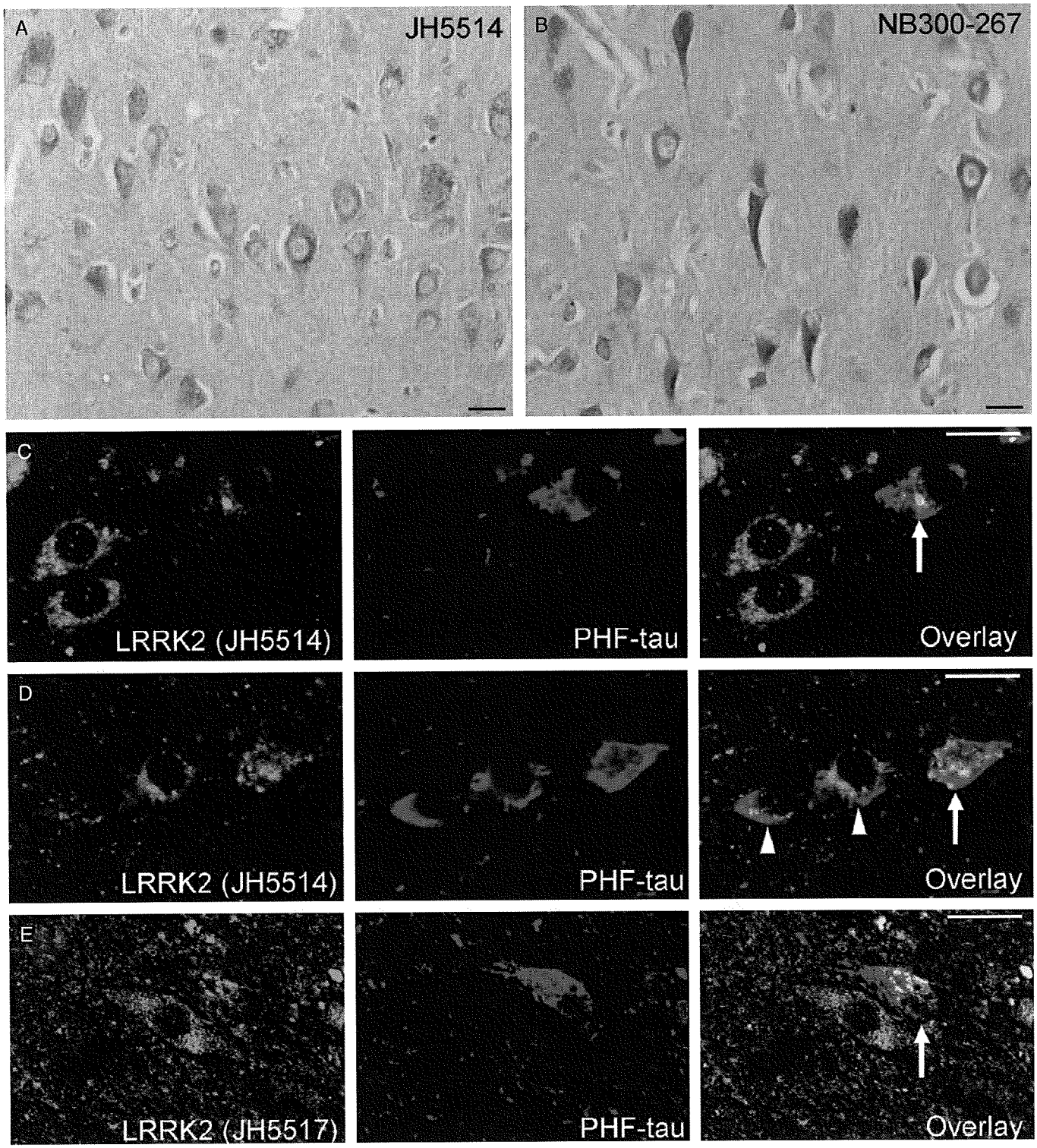

FIGURE 2. Localization of leucine-rich repeat kinase 2 (LRRK2) in brains from Alzheimer disease cases. **(A, B)** The immunoreactivity of LRRK2 in the hippocampal CA region stained with antibody JH5514 **(A)** or NB300-267 **(B)**. **(C–E)** Double immunofluorescent labeling for LRRK2 (**C, D**, JH5514; **E**, JH5517) and paired helical filament (PHF)-tau shows that LRRK2 either does not colocalize (arrowheads) or only partially colocalizes (arrows) with PHF-tau–positive neurofibrillary tangles. Scale bar = 20 μm.

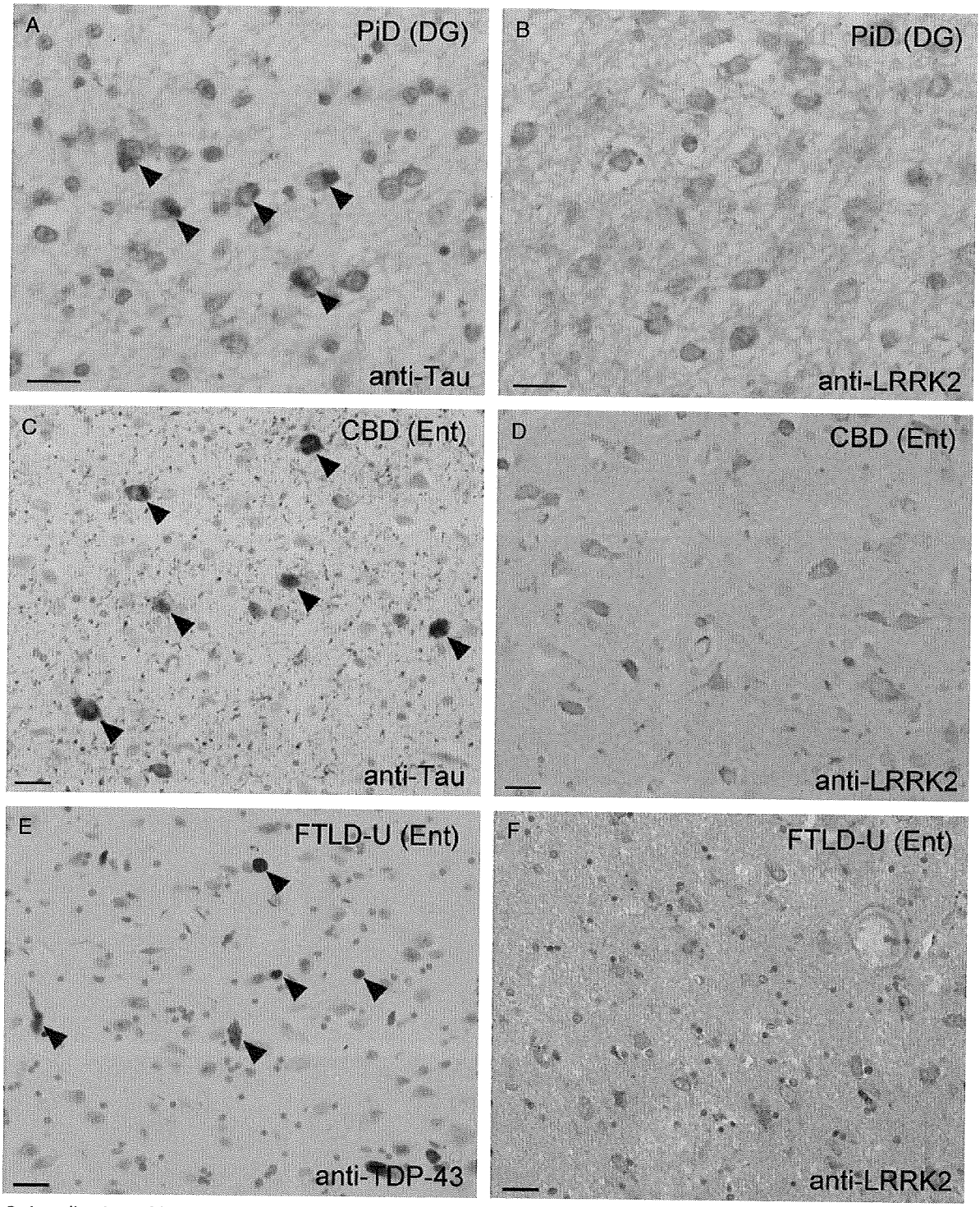

FIGURE 3. Localization of leucine-rich repeat kinase 2 (LRRK2) in various neurodegenerative diseases. **(A, B)** Consecutive paired sections from the dentate gyrus (DG) of a case of Pick disease (PiD) stained with anti–paired helical filament (PHF)-tau **(A)** or anti-LRRK2, NB300-267 antibody **(B)**. Arrowheads in **(A)** indicate tau-positive Pick bodies. **(C, D)** Consecutive sections from the entorhinal cortex (Ent) of a case of corticobasal degeneration (CBD) stained with anti–PHF-tau **(C)** or anti-LRRK2, NB300-267 antibody **(D)**. Arrowheads in **(C)** highlight tau-positive pretangles. **(E, F)** Consecutive sections from the Ent of a case of frontotemporal lobar degeneration with ubiquitin-positive inclusions (FTLD-U) stained with anti–TAR-DNA binding protein 43 (TDP-43) **(E)** or anti-LRRK2, NB300-267 antibody **(F)**. Arrowheads in **(E)** indicate TDP-43–positive dystrophic neurites. **(A)** and **(B)**, **(C)** and **(D)**, and **(E)** and **(F)** are paired consecutive sections obtained from the same affected brain region of a single case for each disorder. Scale bar= 20 μm.

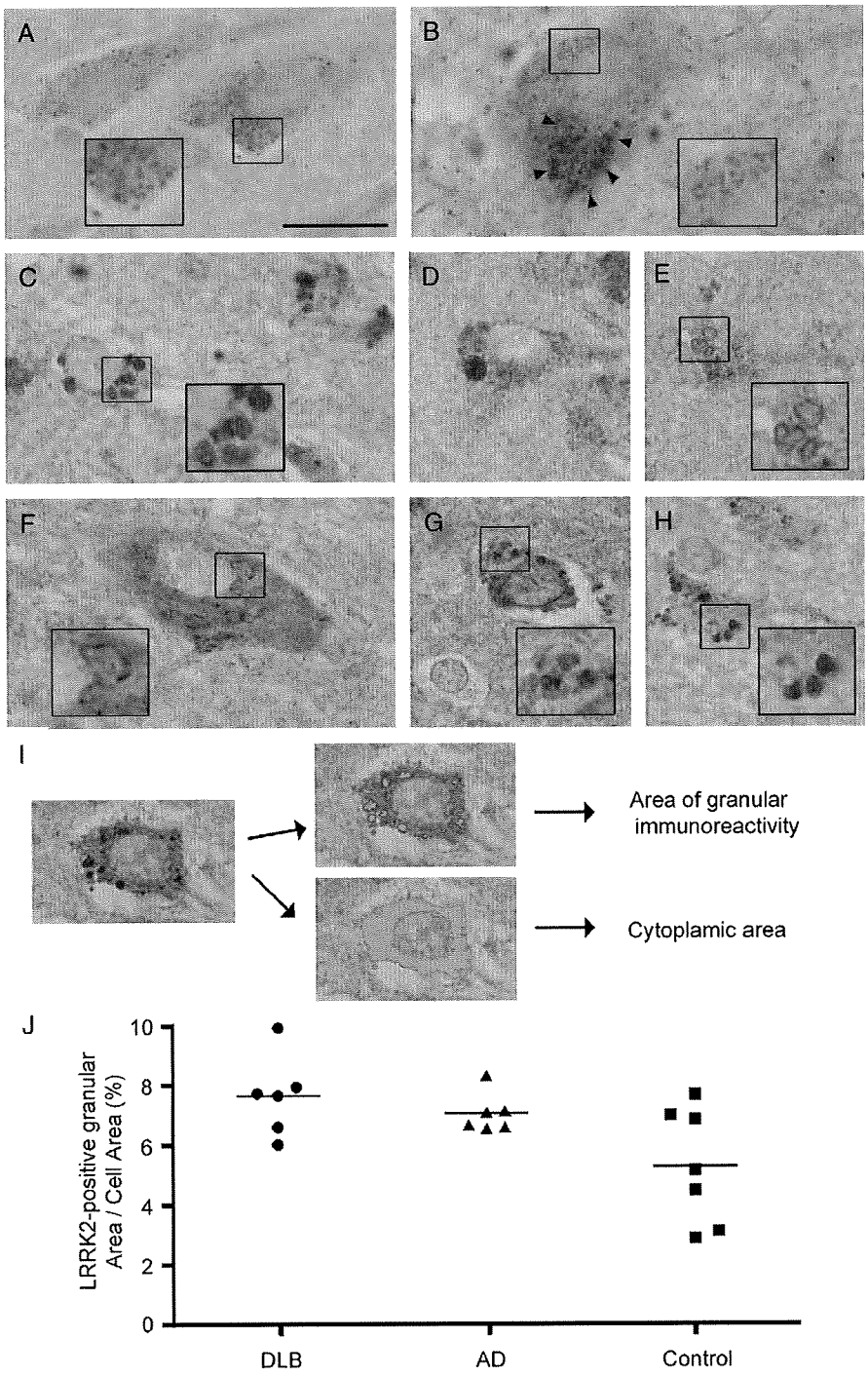

FIGURE 4. Leucine-rich repeat kinase 2 (LRRK2)-positive enlarged granules and vacuoles. **(A, B)** In normal aged controls, LRRK2 immunoreactivity has a small punctate pattern throughout the neuronal soma and processes in the entorhinal cortex **(A)** or neuromelanin-containing dopaminergic neurons (arrowheads) of the substantia nigra pars compacta **(B)**. **(C–E)** In the entorhinal cortex of dementia with Lewy bodies (DLB) cases, LRRK2 immunoreactivity in neurons is mostly in abnormal enlarged **(C)** or giant **(D)** granules or clustered vacuoles **(E)**. **(F, G)** The LRRK2-positive vacuoles or granules in neurons of the substantia nigra pars compacta **(F)** and entorhinal cortex **(G)** from Parkinson disease cases. **(H)** The LRRK2-positive enlarged granules in neurons of the entorhinal cortex from an Alzheimer disease (AD) case. Scale bars **(A–H)** 20 μm. **(I)** Computerized image analysis for estimation of the volume of enlarged granules immunostained with anti-LRRK2 antibody (JH5514) or total cytoplasmic area outlined by brown (diaminobenzidine) immunoreactivity, as described in the Materials and Methods section. **(J)** Percentage of total cell area occupied by LRRK2-positive granules in neurons of the entorhinal cortex of DLB brains (n = 6), AD brains (n = 6), and aged control brains (n = 7). Values are the mean percentage calculated from 25 neurons per brain.

By contrast, LRRK2 immunoreactivity in the hippocampus, entorhinal cortex and amygdala from DLB cases did not appreciably colocalize with phosphorylated α-synuclein-positive cortical-type LBs (data not shown). Instead, LRRK2-positive enlarged granular structures were frequently observed in the cytoplasm of neurons in these brain regions (Fig. 1J). Furthermore, LRRK2-positive dystrophic neurites (DNs) were occasionally observed in PD or DLB brain sections immunostained with the LRRK2 antibody NB300-267 but to a lesser extent compared with phosphorylated α-synuclein–positive DNs (data not shown). The LRRK2-positive DNs were not usually observed in brain sections immunostained with the anti-LRRK2 antibodies JH5517 and JH5514.

With antibody NB300-267, there was robust LRRK2 immunoreactivity that was frequently observed in obvious tangle-bearing neurons of the hippocampus and entorhinal cortex in a subset of AD cases (Fig. 2B); however, LRRK2 immunoreactivity reminiscent of tau-positive NFTs or DNs was not generally observed in these AD cases using antibodies JH5517 and JH5514 (Fig. 2A). Double immunofluorescent labeling using anti–PHF-tau and anti-LRRK2 antibodies (JH5517 and JH5514) revealed that LRRK2 immunoreactivity either does not (Fig. 2D) or only partially (Figs. 2C–E) colocalizes with PHF tau–positive NFTs. We also did not observe LRRK2-positive inclusions in consecutive sections from PiD and corticobasal degeneration brains immunostained for LRRK2 and tau (Figs. 3A–D).

Because tau-negative, α-synuclein–negative, ubiquitin-positive inclusions were reported in brain tissue from a patient with an *LRRK2* mutation (17), we investigated whether LRRK2 localized to TDP-43–positive inclusions in FTLD-U cases. Neither LRRK2-positive inclusions nor dystrophic neurites were observed in consecutive paired sections of brains of FTLD-U cases immunostained for LRRK2 and TDP-43 (Figs. 3E, F).

In summary, these data indicate that LRRK2 is localized to a small subset of brainstem-type LBs but does not localize to other proteinaceous pathological inclusions in the brains of patients with diverse neurodegenerative disorders.

Abnormal Localization of LRRK2 to Enlarged Granules or Vacuoles in Neurons of PD, DLB, and AD Brains

The immunoreactivity of LRRK2 was localized to the neuronal soma and processes in the brains of aged control cases and appeared in a punctate pattern (≤1 μm in diameter) even in regions vulnerable to LB diseases, such as the entorhinal cortex (Fig. 4A) and the substantia nigra pars compacta (Fig. 4B). LRRK2 immunoreactivity frequently localized to numerous dense enlarged granules within neurons of affected regions of DLB brains, such as the entorhinal cortex, amygdala, and to a lesser extent, inferior temporal cortex, using the 3 anti-LRRK2 antibodies (Fig. 1J). These enlarged granules were typically greater than or equal to 1.5 μm in diameter (Fig. 4C) and occasionally greater than 4 μm in diameter (Fig. 4D); they were mostly observed in the neuronal soma but occasionally in neuronal processes. In addition to the enlarged granules, LRRK2 immunoreactivity was often localized to clustered vacuoles in neurons of these limbic regions (Fig. 4E). In PD and DLB brains, the LRRK2-positive enlarged structures are also observed in surviving dopaminergic neurons of the substantia nigra pars compacta (Fig. 4F), but they were not observed in nigral dopaminergic neurons in aged control brains (Fig. 4B). In addition, LRRK2-positive enlarged structures in neurons of the entorhinal cortex were also observed in PD (Fig. 4G) and AD brains (Fig. 4H), albeit to a lesser extent compared with DLB brains. Thus, abnormal neuronal LRRK2 immunoreactivity has similar morphological characteristics in the limbic regions of DLB brains and the substantia nigra pars compacta

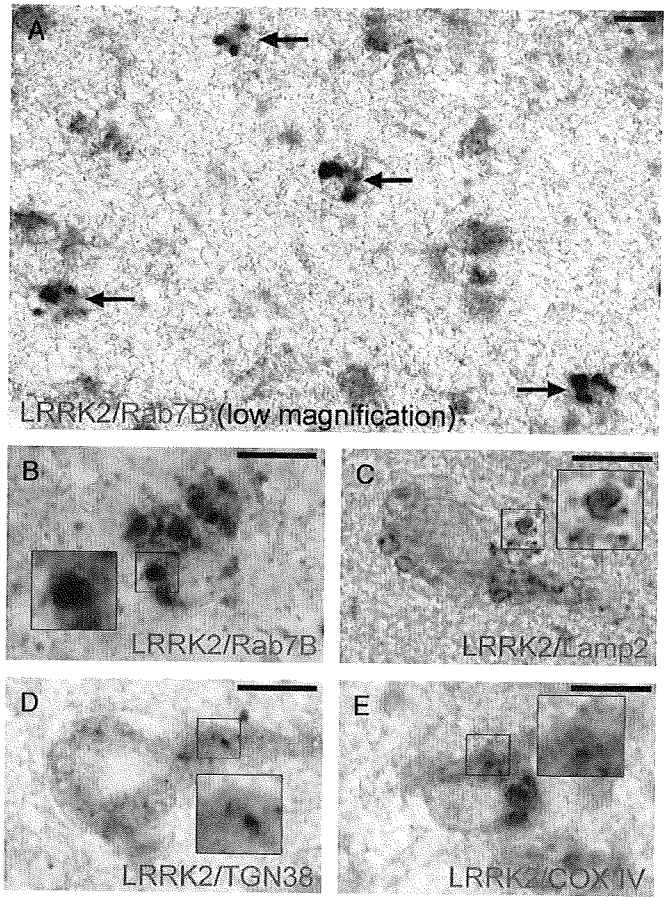

FIGURE 5. Double colorimetric immunolabeling for leucine-rich repeat kinase 2 (LRRK2) and organelle markers in neurons of the entorhinal cortex from cases of dementia with Lewy bodies. **(A, B)** Late-endosome (Rab7B); **(C)** lysosome (lysosomal-associated membrane protein 2 [LAMP-2]); **(D)** trans-Golgi network (TGN38); **(E)** mitochondria (cytochrome oxidase *c* subunit IV [COX IV]). Each color (brown or blue) corresponding to LRRK2 immunoreactivity or organelle marker immunoreactivity is indicated in each image. Insets in **(B–E)** are enlarged regions as indicated. Arrows in **(A)** highlight neurons with double-positive enlarged granules for LRRK2 and Rab7B (dark brown). The LRRK2-positive granules mainly colocalize with Rab7B **(A, B)** and to a lesser extent with LAMP-2 **(C)** but show minimal overlap with TGN38 **(D)** and COX IV **(E)**. Scale bar = 10 μm.

of PD and DLB brains. Therefore, we speculate that these LRRK2-positive enlarged structures may be pathological features common to LB diseases and possibly also AD.

To evaluate the difference in volume of these abnormal granular structures between DLB and AD, we used computerized morphometry to determine the percentages of total neuronal area occupied by LRRK2-positive granular structures in the entorhinal cortex of brains from DLB, AD, and aged control cases. This morphometric analysis enabled a precise estimate of the cell area occupied by granular

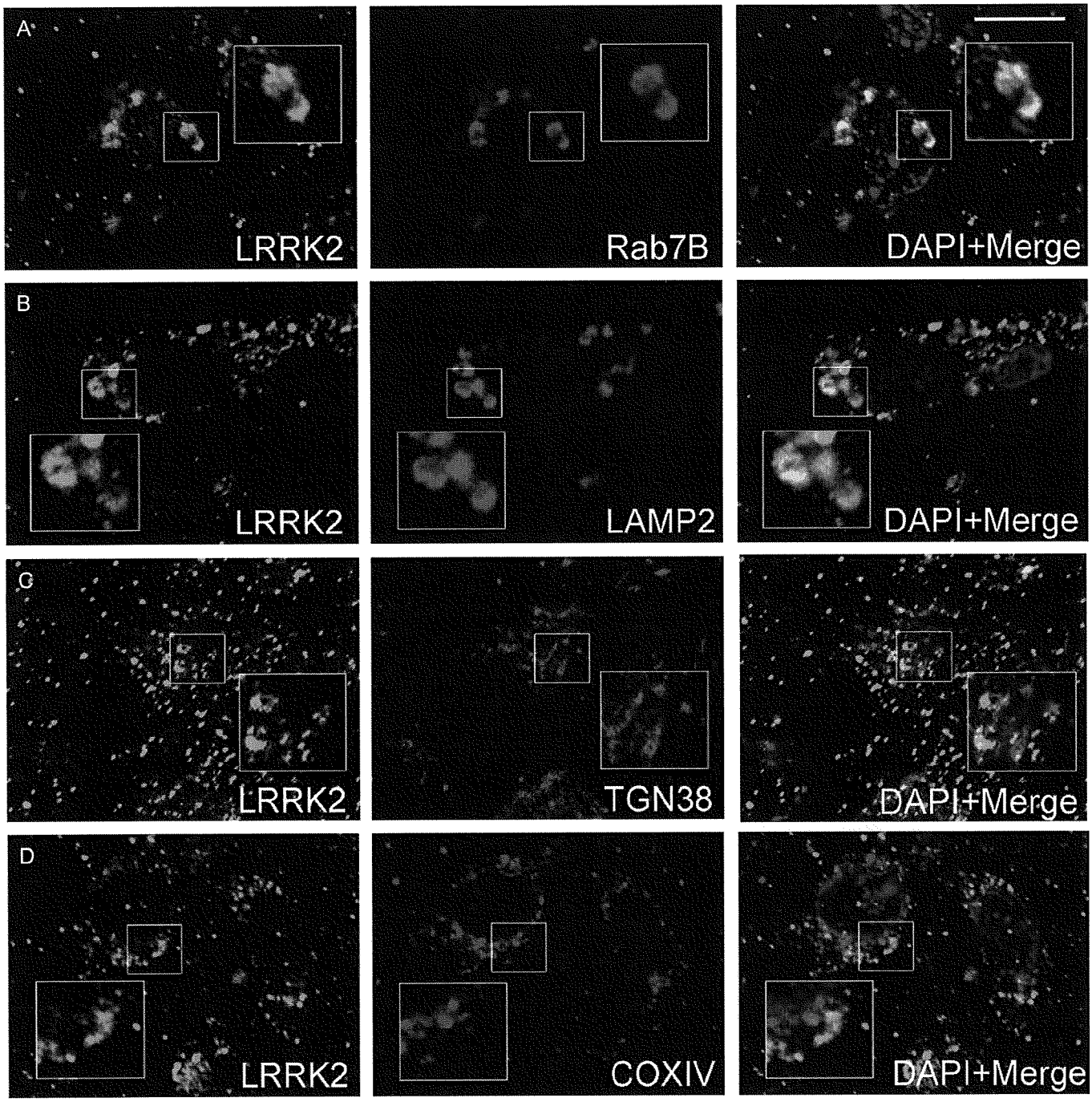

FIGURE 6. Confocal double immunofluorescent images for leucine-rich repeat kinase 2 (LRRK2) and organelle markers in neurons of the entorhinal cortex from cases of dementia with Lewy bodies. **(A)** Late-endosome (Rab7B); **(B)** lysosome (lysosomal-associated membrane protein 2 [LAMP-2]); **(C)** trans-Golgi network (TGN38); **(D)** mitochondria (cytochrome oxidase *c* subunit IV [COX IV]). Insets in **(A–D)** represent enlarged regions as indicated. The LRRK2-positive granules mainly colocalize with Rab7B **(A)** and to a lesser extent with LAMP-2 **(B)** but show minimal overlap with TGN38 **(C)** and COX IV **(D)**. Scale bar = **(A–D)** 10 μm. DAPI, 4′,6-diamidino-2-phenylindole.

LRRK2 immunoreactivity (Fig. 4I). The mean percentage of cell area occupied by granular LRRK2 immunoreactivity was significantly increased in DLB brains compared with control brains (DLB, 7.62% ± 0.55% vs controls, 5.27% ± 0.73% [mean ± SEM], $p = 0.026$) (Fig. 4J). In contrast, there was no significant difference between AD and control brains, despite a strong trend toward increased LRRK2-immunoreactive volumes in the AD brains compared with the control brains (AD, 7.04% ± 0.26%, $p = 0.057$ vs controls) (Fig. 4J). We also analyzed the correlation between cell area occupied by LRRK2-positive granular structures and the stage of neurofibrillary and LB pathology using the Spearman rank correlation coefficient, but the differences were not significant ($p > 0.05$). The LRRK2-positive enlarged structures were only sparsely observed in brains from PiD, progressive supranuclear palsy, corticobasal degeneration, and FTLD-U cases.

LRRK2-Positive Enlarged Granules or Vacuoles Colocalize With Late-Endosomal and Lysosomal Markers, Rab7B and LAMP-2

We next examined the subcellular localization of LRRK2-positive enlarged granules or vacuoles in limbic brain regions from DLB subjects using antibodies to proteins that localize to distinct cytoplasmic organelles. We selected these markers based on the reported localizations of LRRK2 to the Golgi apparatus (35, 40), mitochondria (35, 36, 40), endosomes (35, 41), and lysosomes (35, 42). The LRRK2-positive enlarged granules or vacuoles mostly colocalized with the late endosomal marker, Rab7B (Figs. 5A, 5B, 6A). The proportions of neurons with double-positive granules (LRRK2/Rab7B) in DLB brains varied from case to case: from approximately 5% to 50% (mean ± SD, 24.6% ± 20.9%). The 2 DLB brains with the most severe LB pathology (Stage IV, Table 2) displayed the highest frequency of neurons bearing double-positive granules (49.4% ± 5.9%). Some LRRK2-positive enlarged granules or vacuoles also colocalized with LAMP-2–positive lysosomal structures (Figs. 5C, 6B), albeit in approximately less than 5% of the neurons. In contrast, LRRK2-positive enlarged structures only rarely colocalize with the trans-Golgi marker TGN38 or the mitochondrial marker COX IV (Figs. 5D, E, 6C, D) in neurons of these limbic brain regions from DLB subjects. This indicates that LRRK2 localizes to the endosomal-lysosomal compartment under pathological conditions in LB disease and AD.

DISCUSSION

In the present study, we demonstrate that LRRK2 immunoreactivity colocalizes to a subset of α-synuclein–positive brainstem-type LBs, especially to the inner core and its outer rim of LBs, in PD and DLB brains, whereas α-synuclein immunoreactivity localizes predominantly to the LB halos. In contrast, LRRK2 immunoreactivity does not appreciably overlap with α-synuclein–positive cortical-type LBs and DNs in the cerebral cortex or amygdala of PD and DLB brains. The immunostaining pattern of LRRK2 in LB diseases is clearly distinct from that of α-synuclein and tends to resemble that of synphilin 1 (43). In contrast to the LB halo, which is composed of Lewy filaments, the core of LBs is mainly composed of densely packed vesicular structures (44). Therefore, we speculate that LRRK2 might localize to vesicular structures of unknown origin rather than to filamentous aggregates of α-synuclein within LBs, as has also been speculated for synphilin 1 localization (43).

We also found that LRRK2 immunoreactivity did not colocalize with tau-positive NFTs, other tau inclusions, or with TDP-43–positive inclusions in brains of AD, various tauopathies or TDP-43 proteinopathy cases. In AD brains, LRRK2 immunoreactivity did not localize to NFTs when the anti-LRRK2 antibodies JH5517 and JH5514 were used, whereas it localized with a subset of NFTs when the commercial anti-LRRK2 antibody NB300-267 was used. The 3 distinct rabbit polyclonal antibodies to LRRK2 used here were rigorously evaluated in our previous study, in which we show that each antibody can detect endogenous human LRRK2 protein (38). The inconsistent findings between the JH5514 and JH5517 antibodies and the NB300-267 antibody may be caused by additional non-specific cross reactivity of NB300-267 because the JH5514 antibody has been validated using LRRK2-knockout mice and detects endogenous LRRK2 as the major protein species in brain tissue in wild-type control mice (38). We conclude, therefore, that LRRK2 is not a component common to different protein aggregates of these neurodegenerative disorders.

We next examined whether the subcellular localization or expression of LRRK2 is altered under pathological conditions in neurodegenerative disease. We previously reported that LRRK2 localizes exclusively to neuronal membrane-bound and vesicular structures including endosomes, lysosomes, multivesicular bodies, various transport vesicles, and mitochondria in vivo (35). In addition, LRRK2 immunoreactivity is morphologically observed as a distinct punctate staining pattern in human and rodent brain tissues and mouse primary cortical neurons (19, 35), consistent with the present data in aged human control brains. In the present study, morphological alterations of LRRK2 immunoreactivity were frequently observed as enlarged granules or clustered vacuoles in neurons within the affected limbic areas of DLB brains. Morphometric analysis reveals that the volume of cell area occupied by these LRRK2-positive structures in neurons was elevated in brain regions with LB pathology in DLB compared with similar regions of aged control brains. Recent studies have shown that certain disease-linked mutations in *LRRK2* produce a hyperactive kinase and induce toxicity in primary neurons (36, 40, 45, 46). In addition, autosomal-dominant inheritance of *LRRK2* mutations in families with PD is most likely consistent with a gain-of-function mechanism for the pathogenic properties of *LRRK2* mutations (47). Therefore, it is most likely that morphological alterations and increased volume of LRRK2 immunoreactivity may reflect an elevated expression level and thus greater overall kinase or enzymatic activity of LRRK2 per neuron in brain regions with Lewy pathology. At this juncture, however, it is not possible to rule out improved accessibility of LRRK2 epitopes for binding to each antibody

that would also result in increased LRRK2 immunoreactivity in brain tissue. This seems unlikely because the 3 antibodies we used detect distinct amino- or carboxyl-terminal epitopes. Because it has been exceedingly difficult to detect full-length LRRK2 in postmortem human samples by Western analysis with numerous LRRK2 antibodies, it is not currently possible to determine whether there is an increase in LRRK2 protein expression in these DLB brain regions. This issue will require further analysis as the tools for detecting LRRK2 improve.

The LRRK2-positive enlarged granules or vacuoles frequently colocalized to Rab7B-positive late endosomes and occasionally with LAMP-2–positive lysosomes, suggesting that LRRK2 may be associated with the endosomal-lysosomal system in these pathological brains. Growing evidence indicates that the autophagy or lysosomal systems are associated with the pathogenesis of PD, including accumulation of autophagic vacuoles in PD brains (48), clearance of misfolded α-synuclein by autophagy (49–51), and mutations in the lysosomal ATPase *ATP13A2* leading to a parkinsonian phenotype (7). In addition, there is recent evidence of an important role for LRRK2 in the endosomal-lysosomal system. For example, increased autophagic or lysosomal compartments were observed in primary cortical neurons (52) and in SH-SY5Y cells expressing the *LRRK2* G2019S variant (42). Moreover, LRRK2 is reported to interact with Rab5B, a component of the endosomal pathway that regulates synaptic vesicle endocytosis (41). Shin et al (41) recently demonstrated that LRRK2 overexpression impaired synaptic vesicle endocytosis in rat primary hippocampal neurons, indicating that LRRK2 may influence endosomal pathway function (39). These observations suggest that PD-linked mutations in *LRRK2* may lead to neuronal dysfunction and parkinsonism through perturbations in the endosomal-lysosomal trafficking pathway. Given that LRRK2 is localized to the core of LBs that are typically enriched in vesicular structures as previously described, localization of LRRK2 to the endosomal-lysosomal subcellular compartments within neurons suggests that LRRK2 may function as part of the endocytic machinery that normally regulates vesicular trafficking.

Intriguingly, LRRK2-positive enlarged structures are also observed in neurons of the limbic area of AD brains. The volume of cell area occupied by LRRK2-positive structures in neurons of AD brains showed a strong tendency to increase compared with that in aged control brains; however, this was not statistically significant. Involvement of the endosomal-lysosomal system in the pathogenesis of AD is well documented, and expression of various endosomal or lysosomal proteins are reported to be increased in neurons in regions affected in AD (53, 54). Late endosome/multivesicular bodies contain amyloid-β (Aβ) peptide (55), and intracellular Aβ peptide may be generated in the endosomal compartment by cleavage of amyloid precursor protein (56). In addition, with reference to abnormalities of the endosomal-lysosomal system in several neurodegenerative disorders (57), recent studies suggest that impaired autophagy through genetic disruption of ATG5 or ATG7 in neurons causes frank neuronal degeneration characterized by ubiquitin-positive inclusions, a pathological feature common to many neurodegenerative disorders (58, 59). Thus, disruption of the endosomal-lysosomal system is considered to be a pathogenic event common not only to LB diseases such as PD and DLB, but also to other neurodegenerative disorders including AD, as suggested by our finding of abnormal LRRK2-positive enlarged late endosomal compartments in neurons of the limbic area of AD brains and in DLB brains. Because *LRRK2* mutations usually cause a PD phenotype, however, the involvement of LRRK2 in the pathogenesis of AD may be indirect. It is of great interest to determine whether the function of LRRK2 in the endosomal machinery is associated with the pathogenesis of AD or with the diverse pathology observed in brains with *LRRK2* mutations.

In conclusion, the present observation that LRRK2 is localized only to the core of α-synuclein–positive brainstem-type LBs but not to α-synuclein–positive cortical-type LBs and DNs, tau-positive NFTs and other inclusions, or TDP-43–positive inclusions suggests that LRRK2 is not a common cardinal protein component of filamentous proteinaceous aggregates in various neurodegenerative disorders. In addition, morphological alterations and increased volume of LRRK2 immunoreactivity in DLB brains may indicate perturbed expression or enzymatic activity of LRRK2 associated with Lewy pathology and could be associated with a principal pathogenic event that triggers the development of the disease. The present observation that LRRK2-positive granules or vacuoles colocalize with the endosomal-lysosomal compartment may be associated with the pathogenic role of LRRK2 leading to neuronal degeneration. These findings may provide important insight into the contribution of LRRK2 dysfunction to the pathogenesis of LB diseases.

ACKNOWLEDGMENTS

The authors thank the patients and their families who made this research possible. Ted M. Dawson is the Leonard and Madlyn Abramson Professor in Neurodegenerative Diseases at Johns Hopkins.

REFERENCES

1. Polymeropoulos MH, Lavedan C, Leroy E, et al. Mutation in the alpha-synuclein gene identified in families with Parkinson's disease. Science 1997;276:2045–47
2. Kitada T, Asakawa S, Hattori N, et al. Mutations in the *parkin* gene cause autosomal recessive juvenile parkinsonism. Nature 1998;392:605–8
3. Valente EM, Abou-Sleiman PM, Caputo V, et al. Hereditary early-onset Parkinson's disease caused by mutations in PINK1. Science 2004;304:1158–60
4. Bonifati V, Rizzu P, van Baren MJ, et al. Mutations in the DJ-1 gene associated with autosomal recessive early-onset parkinsonism. Science 2003;299:256–59
5. Zimprich A, Biskup S, Leitner P, et al. Mutations in LRRK2 cause autosomal-dominant parkinsonism with pleomorphic pathology. Neuron 2004;44:601–7
6. Paisan-Ruiz C, Jain S, Evans EW, et al. Cloning of the gene containing mutations that cause PARK8-linked Parkinson's disease. Neuron 2004;44:595–600
7. Ramirez A, Heimbach A, Grundemann J, et al. Hereditary parkinsonism with dementia is caused by mutations in ATP13A2, encoding a lysosomal type 5 P-type ATPase. Nat Genet 2006;38:1184–91
8. Gilks WP, Abou-Sleiman PM, Gandhi S et al. A common LRRK2 mutation in idiopathic Parkinson's disease. Lancet 2005;365:415–16

9. Kachergus J, Mata IF, Hulihan M, et al. Identification of a novel LRRK2 mutation linked to autosomal dominant parkinsonism: Evidence of a common founder across European populations. Am J Hum Genet 2005; 76:672–80
10. Healy DG, Falchi M, O'Sullivan SS, et al. Phenotype, genotype, and worldwide genetic penetrance of LRRK2-associated Parkinson's disease: A case-control study. Lancet Neurol 2008;7:583–90
11. Hulihan MM, Ishihara-Paul L, Kachergus J, et al. LRRK2 Gly2019Ser penetrance in Arab-Berber patients from Tunisia: A case-control genetic study. Lancet Neurol 2008;7:591–94
12. Giasson BI, Covy JP, Bonini NM, et al. Biochemical and pathological characterization of Lrrk2. Ann Neurol 2006;59:315–22
13. Giordana MT, D'Agostino C, Albani G, et al. Neuropathology of Parkinson's disease associated with the LRRK2 Ile1371Val mutation. Mov Disord 2007;22:275–78
14. Ross OA, Toft M, Whittle AJ, et al. Lrrk2 and Lewy body disease. Ann Neurol 2006;59:388–93
15. Wszolek ZK, Pfeiffer RF, Tsuboi Y, et al. Autosomal dominant parkinsonism associated with variable synuclein and tau pathology. Neurology 2004;62:1619–22
16. Rajput A, Dickson DW, Robinson CA, et al. Parkinsonism, Lrrk2 G2019S, and tau neuropathology. Neurology 2006;67:1506–8
17. Dachsel JC, Ross OA, Mata IF, et al. Lrrk2 G2019S substitution in frontotemporal lobar degeneration with ubiquitin-immunoreactive neuronal inclusions. Acta Neuropathol 2007;113:601–6
18. Hasegawa K, Kowa H. Autosomal dominant familial Parkinson disease: Older onset of age, and good response to levodopa therapy. Eur Neurol 1997;38(suppl 1):39–43
19. Higashi S, Biskup S, West AB, et al. Localization of Parkinson's disease-associated LRRK2 in normal and pathological human brain. Brain Res 2007;1155:208–19
20. Higashi S, Moore DJ, Colebrooke RE, et al. Expression and localization of Parkinson's disease–associated leucine-rich repeat kinase 2 in the mouse brain. J Neurochem 2007;100:368–81
21. Galter D, Westerlund M, Carmine A, et al. LRRK2 expression linked to dopamine-innervated areas. Ann Neurol 2006;59:714–19
22. Taymans JM, Van den Haute C, Baekelandt V. Distribution of PINK1 and LRRK2 in rat and mouse brain. J Neurochem 2006;98:951–61
23. Melrose H, Lincoln S, Tyndall G, et al. Anatomical localization of leucine-rich repeat kinase 2 in mouse brain. Neuroscience 2006;139: 791–94
24. Melrose HL, Kent CB, Taylor JP. A comparative analysis of leucine-rich repeat kinase 2 (Lrrk2) expression in mouse brain and Lewy body disease. Neuroscience 2007;147:1047–58
25. Perry G, Zhu X, Babar AK, et al. Leucine-rich repeat kinase 2 colocalizes with alpha-synuclein in Parkinson's disease, but not tau-containing deposits in tauopathies. Neurodegener Dis 2008;5:222–24
26. Zhu X, Babar A, Siedlak SL, et al. LRRK2 in Parkinson's disease and dementia with Lewy bodies. Mol Neurodegener 2006;1:17
27. Zhu X, Siedlak SL, Smith MA et al. LRRK2 protein is a component of Lewy bodies. Ann Neurol 2006;60:617–8; [author reply 618–19]
28. Miklossy J, Arai T, Guo JP, et al. LRRK2 expression in normal and pathologic human brain and in human cell lines. J Neuropathol Exp Neurol 2006;65:953–63
29. Gelb DJ, Oliver E, Gilman S. Diagnostic criteria for Parkinson disease. Arch Neurol 1999;56:33–39
30. McKeith IG, Dickson DW, Lowe J, et al. Diagnosis and management of dementia with Lewy bodies: Third report of the DLB Consortium. Neurology 2005;65:1863–72
31. Consensus recommendations for the postmortem diagnosis of Alzheimer's disease. The National Institute on Aging, and Reagan Institute Working Group on Diagnostic Criteria for the Neuropathological Assessment of Alzheimer's Disease. Neurobiol Aging 1997;18:S1–S2
32. Higashi S, Iseki E, Yamamoto R, et al. Concurrence of TDP-43, tau and alpha-synuclein pathology in brains of Alzheimer's disease and dementia with Lewy bodies. Brain Res 2007;1184:284–94
33. Braak H, Alafuzoff I, Arzberger T, et al. Staging of Alzheimer disease–associated neurofibrillary pathology using paraffin sections and immunocytochemistry. Acta Neuropathol (Berl) 2006;112:389–404
34. Marui W, Iseki E, Kato M, et al. Pathological entity of dementia with Lewy bodies and its differentiation from Alzheimer's disease. Acta Neuropathol (Berl) 2004;108:121–28
35. Biskup S, Moore DJ, Celsi F, et al. Localization of LRRK2 to membranous and vesicular structures in mammalian brain. Ann Neurol 2006; 60:557–69
36. West AB, Moore DJ, Biskup S, et al. Parkinson's disease–associated mutations in leucine-rich repeat kinase 2 augment kinase activity. Proc Natl Acad Sci U S A 2005;102:16842–47
37. Greggio E, Jain S, Kingsbury A, et al. Kinase activity is required for the toxic effects of mutant LRRK2/dardarin. Neurobiol Dis 2006;23:329–41
38. Biskup S, Moore DJ, Rea A, et al. Dynamic and redundant regulation of LRRK2 and LRRK1 expression. BMC Neurosci 2007;8:102
39. Saito Y, Kawashima A, Ruberu NN, et al. Accumulation of phosphorylated alpha-synuclein in aging human brain. J Neuropathol Exp Neurol 2003;62:644–54
40. Gloeckner CJ, Kinkl N, Schumacher A, et al. The Parkinson disease causing LRRK2 mutation I2020T is associated with increased kinase activity. Hum Mol Genet 2006;15:223–32
41. Shin N, Jeong H, Kwon J, et al. LRRK2 regulates synaptic vesicle endocytosis. Exp Cell Res 2008;314:2055–65
42. Plowey ED, Cherra SJ 3rd, Liu YJ, et al. Role of autophagy in G2019S-LRRK2–associated neurite shortening in differentiated SH-SY5Y cells. J Neurochem 2008;105:1048–56
43. Wakabayashi K, Engelender S, Yoshimoto M, et al. Synphilin-1 is present in Lewy bodies in Parkinson's disease. Ann Neurol 2000;47: 521–23
44. Takahashi H, Wakabayashi K. The cellular pathology of Parkinson's disease. Neuropathology 2001;21:315–22
45. Smith WW, Pei Z, Jiang H, et al. Kinase activity of mutant LRRK2 mediates neuronal toxicity. Nat Neurosci 2006;9:1231–33
46. West AB, Moore DJ, Choi C, et al. Parkinson's disease–associated mutations in LRRK2 link enhanced GTP-binding and kinase activities to neuronal toxicity. Hum Mol Genet 2007;16:223–32
47. Moore DJ. The biology and pathobiology of LRRK2: Implications for Parkinson's disease. Parkinsonism Relat Disord 2008;14(suppl 2): S92–98
48. Anglade P, Vyas S, Javoy-Agid F, et al. Apoptosis and autophagy in nigral neurons of patients with Parkinson's disease. Histol Histopathol 1997;12:25–31
49. Cuervo AM, Stefanis L, Fredenburg R, et al. Impaired degradation of mutant alpha-synuclein by chaperone-mediated autophagy. Science 2004;305:1292–95
50. Lee HJ, Khoshaghideh F, Patel S et al. Clearance of alpha-synuclein oligomeric intermediates via the lysosomal degradation pathway. J Neurosci 2004;24:1888–96
51. Webb JL, Ravikumar B, Atkins J, et al. Alpha-synuclein is degraded by both autophagy and the proteasome. J Biol Chem 2003;278:25009–13
52. MacLeod D, Dowman J, Hammond R, et al. The familial parkinsonism gene *LRRK2* regulates neurite process morphology. Neuron 2006;52: 587–93
53. Cataldo AM, Barnett JL, Pieroni C, et al. Increased neuronal endocytosis and protease delivery to early endosomes in sporadic Alzheimer's disease: Neuropathologic evidence for a mechanism of increased beta-amyloidogenesis. J Neurosci 1997;17:6142–51
54. Nixon RA, Wegiel J, Kumar A, et al. Extensive involvement of autophagy in Alzheimer disease: An immuno-electron microscopy study. J Neuropathol Exp Neurol 2005;64:113–22
55. Takahashi RH, Milner TA, Li F, et al. Intraneuronal Alzheimer abeta42 accumulates in multivesicular bodies and is associated with synaptic pathology. Am J Pathol 2002;161:1869–79
56. Small SA, Gandy S. Sorting through the cell biology of Alzheimer's disease: Intracellular pathways to pathogenesis. Neuron 2006;52:15–31
57. Martinez-Vicente M, Cuervo AM. Autophagy and neurodegeneration: When the cleaning crew goes on strike. Lancet Neurol 2007;6:352–61
58. Hara T, Nakamura K, Matsui M, et al. Suppression of basal autophagy in neural cells causes neurodegenerative disease in mice. Nature 2006;441: 885–89
59. Komatsu M, Waguri S, Chiba T, et al. Loss of autophagy in the central nervous system causes neurodegeneration in mice. Nature 2006;441: 880–84

Biochemical and Biophysical Research Communications 387 (2009) 121–126

Contents lists available at ScienceDirect

Biochemical and Biophysical Research Communications

journal homepage: www.elsevier.com/locate/ybbrc

Familial amyotrophic lateral sclerosis-linked mutant SOD1 aberrantly interacts with tubulin

Tomohiro Kabuta [a,*], Aiko Kinugawa [a], Yukihiro Tsuchiya [a], Chihana Kabuta [a], Rieko Setsuie [a], Minako Tateno [b], Toshiyuki Araki [b], Keiji Wada [a,*]

[a] Department of Degenerative Neurological Diseases, National Institute of Neuroscience, National Center of Neurology and Psychiatry, Kodaira, Tokyo 187-8502, Japan
[b] Department of Peripheral Nervous System Research, National Institute of Neuroscience, National Center of Neurology and Psychiatry, Kodaira, Tokyo 187-8502, Japan

ARTICLE INFO

Article history:
Received 19 June 2009
Available online 1 July 2009

Keywords:
SOD1
ALS
Tubulin
Interaction

ABSTRACT

Mutations in the Cu,Zn-superoxide dismutase (SOD1) gene cause 20–25% of familial amyotrophic lateral sclerosis (ALS). Mutant SOD1 causes motor neuron degeneration through toxic gain-of-function(s). However, the direct molecular targets of mutant SOD1, underlying its toxicity, are not fully understood. In this study, we found that α/β-tubulin is one of the major mutant SOD1-interacting proteins, but that wild-type SOD1 does not interact with it. The interaction between tubulin and mutant SOD1 was detected in the spinal cords of mutant G93A SOD1 transgenic mice before the onset of symptoms. Tubulin interacted with amino acid residues 1–23 and 116–153 of SOD1. Overexpression of mutant SOD1 resulted in the accumulation of tubulin in detergent-insoluble fractions. In a cell-free system, mutant SOD1 modulated tubulin polymerization, while wild-type SOD1 did not. Since tightly regulated microtubule dynamics is essential for neurons to remain viable, α/β-tubulin could be an important direct target of mutant SOD1.

Introduction

Amyotrophic lateral sclerosis (ALS) is a fatal neurodegenerative disease caused by selective loss of motor neurons. Five to 10 percent of ALS cases are known to occur in familial forms. Dominant missense mutations in the gene that encodes the Cu/Zn-superoxide dismutase, SOD1, are associated with 20–25% of familial ALS cases (fALS). Mice overexpressing mutant SOD1 develop an ALS-like phenotype and have been used as a mouse model of ALS, whereas mice lacking SOD1 do not [1,2]. These studies indicate that mutant SOD1 causes motor neuron degeneration not by loss of function of SOD1, but by toxic gain-of-function(s) of mutant SOD1.

The toxic properties of mutant SOD1 may be exerted at least partly through the physical interactions of mutant SOD1 with other functional proteins. Recent studies suggest that the physical interactions of mutant SOD1 with other cellular proteins, such as Derlin-1, mediate the toxicity of mutant SOD1 [3]. However, the direct molecular targets of mutant SOD1, underlying its toxicity, are not fully understood. Therefore, elucidating novel mutant SOD1-interacting proteins is important for understanding the mechanisms that underlie the pathology of ALS, and for developing effective therapies for ALS.

In this study, we sought to identify novel mutant SOD1-interacting proteins using coimmunoprecipitation assays and mass spectrometry analyses. We found that α/β-tubulin is one of the major mutant SOD1-interacting proteins.

Materials and methods

Plasmid constructs and antibodies. These reagents are described in the Supplemental materials and methods.

Cell culture and transfection. HeLa, COS-7 and Neuro2a cells were maintained in Dulbecco's modified Eagle's medium (Sigma, St. Louis, MO) supplemented with 10% fetal bovine serum (JRH Biosciences, Lenexa, KS). Transient expression of each vector in cells was performed using Lipofectamine LTX (Invitrogen) or the FuGENE 6 transfection reagent (Roche, Indianapolis, IN). Differentiation of Neuro2a cells was induced by adding 5 mM dibutyryl cAMP, 4 h after transfection, as described previously [4].

Preparation of recombinant proteins. Recombinant SOD1 proteins were prepared according to methods described previously [4]. Detailed procedures are described in the Supplemental materials and methods.

Immunoprecipitation. Immunoprecipitation was performed as previously described [5]. Detailed procedures are described in the Supplemental materials and methods.

* Corresponding authors. Fax: +81 42 346 1745.
E-mail addresses: kabuta@ncnp.go.jp (T. Kabuta), wada@ncnp.go.jp (K. Wada).

0006-291X/$ - see front matter © 2009 Elsevier Inc. All rights reserved.
doi:10.1016/j.bbrc.2009.06.138

Mutant G93A SOD1 transgenic mice. Transgenic mice expressing G93A hSOD1 (G1L line of B6SJL-TgN(SOD1-G93A)1Gur^{dl}) were obtained from the Jackson Laboratory (Bar Harbor, ME), and backcrossed to C57BL/6J for more than 14 generations. These mice were propagated at the National Institute of Neuroscience, National Center of Neurology and Psychiatry. We observed that the G93A SOD1-transgenic mice we used in this study experienced disease onset around the age of 8 months (246.5 ± 5.8 days) and died around 9.5 months (288.5 ± 7.1. days, mean ± SEM, $n = 14$). For coimmunoprecipitation assays, brains and spinal cords from male mice at 65 days of age were homogenized in immunoprecipitation buffer. After the lysates were centrifuged at 20,000 *g* for 10 min at 4 °C, 1 ml of the supernatants (~1.5 mg/ml protein in immunoprecipitation buffer) were incubated with 15 μg of antibody for 15 h, and immunoprecipitation was performed using protein G Sepharose. All experiments using mice were approved by the institution's Animal Investigation Committee.

Immunoblotting analysis. SDS–PAGE was performed under reducing conditions. Immunoblotting was performed according to standard procedures as described previously [6]. The preparation of detergent (1% Triton X-100)-soluble and -insoluble fractions was performed as described previously [6].

Mass spectrometry analysis. Protein bands (55-kDa proteins in Fig. 1A) were sliced from gel and subjected to in-gel trypsin digestion, and liquid chromatography–tandem mass spectrometry (LC–MS/MS) analysis was performed at Shimadzu (Kyoto, Japan) as a custom service.

Pull-down assay. A pull-down assay was performed as described previously [4]. Detailed procedures are described in the Supplemental materials and methods.

Tubulin polymerization assay. An in vitro tubulin polymerization assay was performed using a Tubulin Polymerization Assay kit, OD based, >99% pure tubulin (Cytoskeleton), according to the manufacturer's protocol. Recombinant SOD1 without a tag and tubulin were mixed to give a final concentration of ~0.04 mg/ml SOD1 and 3 mg/ml tubulin in tubulin polymerization buffer (80 mM PIPES, pH 6.9, 2 mM $MgCl_2$, 0.5 mM EGTA, 1 mM GTP, 5% glycerol), and subjected to a tubulin polymerization assay. As a control, vehicle was added instead of SOD1.

Statistical analysis. For comparison of two groups, the statistical difference was determined by the Student's *t*-test. For comparison

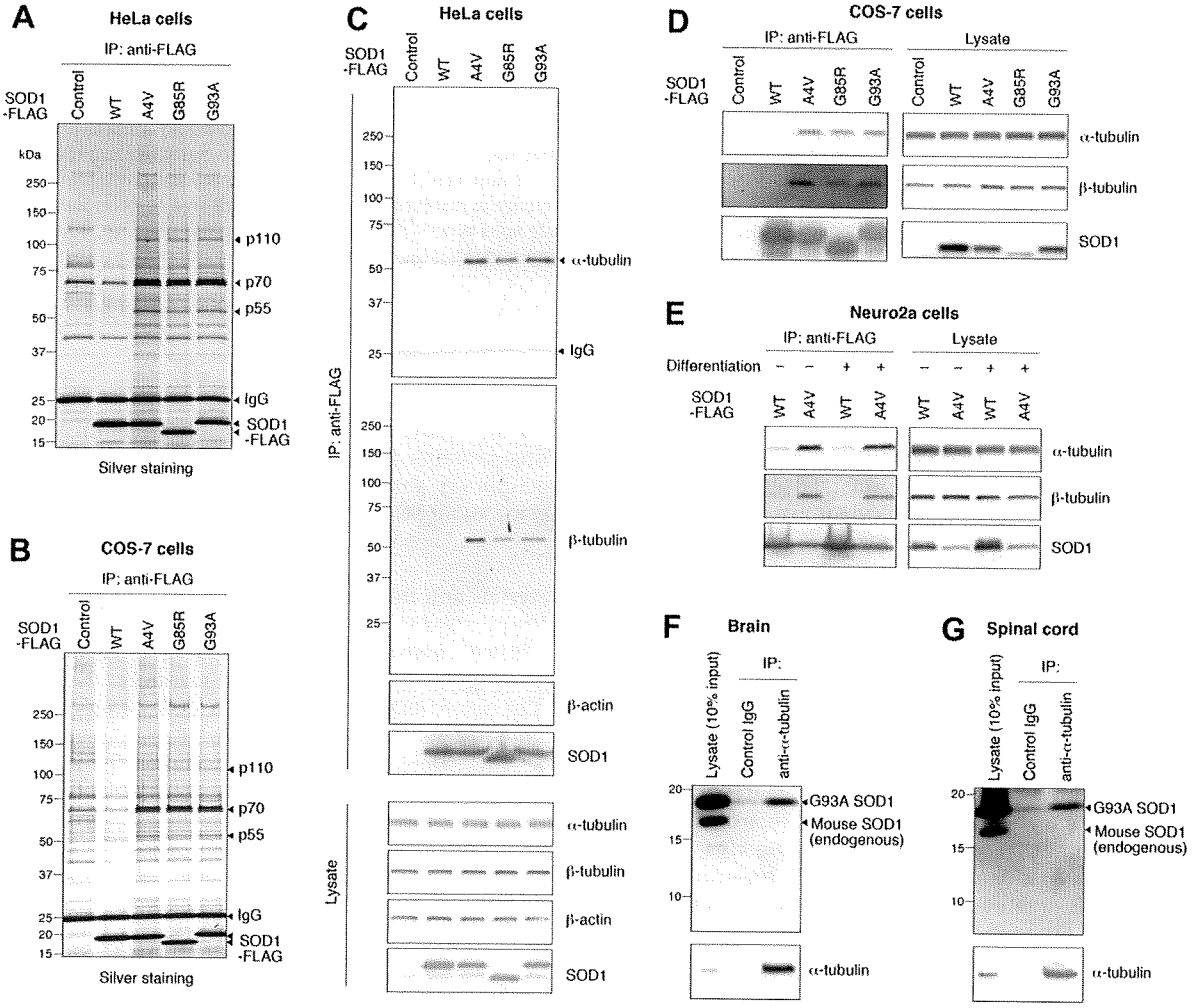

Fig. 1. Interaction between mutant SOD1 and tubulin. (A,B) Lysates of HeLa cells (A) or COS-7 cells (B) transfected with the indicated constructs (Control: empty vector) were immunoprecipitated with anti-FLAG antibody. The immunoprecipitants were analyzed by SDS–PAGE followed by silver staining. In the presence of FLAG-tagged mutant SOD1, mutant SOD1-interacting proteins were coimmunoprecipitated with mutant SOD1, while in the absence of mutant SOD1, proteins were nonspecifically precipitated with anti-FLAG beads. (C–E) HeLa (C), COS-7 (D) or Neuro2a (E) cells were transfected with the indicated constructs. Differentiation of Neuro2a cells was induced by adding 5 mM dibutyryl cAMP. Immunoprecipitation was performed using anti-FLAG antibody. The lysates and immunoprecipitants were analyzed by immunoblotting. (F,G) Lysates were prepared from the brains (F) and spinal cords (G) of mutant G93A transgenic mouse, and immunoprecipitated with anti-α-tubulin antibody or control IgG. The lysates and immunoprecipitants were analyzed by immunoblotting. Mutant SOD1 was clearly precipitated with α-tubulin. The coimmunoprecipitation of mutant SOD1 was also observed when immunoprecipitation was performed using anti-β-tubulin antibody (data not shown).

of more than two groups, Dunnett's multiple comparison test was used.

Results

Mutant SOD1 interacts with α/β-tubulin

To understand the molecular mechanism underlying the gain-of-toxicity of mutant SOD1, we attempted to identify proteins that interact with mutant SOD1 using a coimmunoprecipitation assay. We observed that the SOD1 mutants specifically interacted with multiple proteins, although wild-type SOD1 did not (Fig. 1A). Among these interacting proteins, the band intensities of the 110-kDa, 70-kDa and 55-kDa proteins were considerably higher than those of other interacting proteins (Fig. 1A). The interactions of theses proteins with mutant SOD1 were also detected when we used COS-7 or Neuro2a cells (Fig. 1B and 3C).

The 110-kDa protein interacting with mutant SOD1 was previously reported to be heat-shock protein 105 [7]; mutant SOD1 was also previously reported to interact with the 70 kDa heat shock protein 70 and heat shock cognate protein 70 [8]. Using LC–MS/MS analysis, we confirmed that the 70-kDa band contained heat shock cognate protein 70 (data not shown). Using LC–MS/MS analysis, we found that the 55-kDa proteins interacting with mutant SOD1 in Fig. 1A are human α-tubulin and β-tubulin (Supplemental Fig. 1A and Supplemental files 1 and 2), indicating that mutant SOD1 physically interacts with endogenous α-tubulin and β-tubulin. The interactions of mutant SOD1 with α-tubulin and β-tubulin were also detected by immunoblotting (Fig. 1C). Consistent with the silver staining analysis (Fig. 1A), an interaction of wild-type SOD1 with tubulin was not detected (Fig. 1C). The interaction between mutant SOD1 and endogenous tubulin was also observed in COS-7 cells, and in both undifferentiated and differentiated Neuro2a cells (Fig. 1D and E). In contrast to tubulin, an interaction of β-actin with mutant SOD1 was not observed (Fig. 1C), indicating that the interaction between mutant SOD1 and tubulin is not a non-specific interaction of abundant proteins.

To confirm the interaction of mutant SOD1 with tubulin *in vivo*, we performed coimmunoprecipitation assays using the spinal cords and brains of G93A SOD1 transgenic mice before the onset of the symptoms. The interaction of tubulin with G93A SOD1, but not with mouse wild-type SOD1, was clearly detected in the spinal cords and brains (Fig. 1F and G). Since the interaction between mutant SOD1 and tubulin was observed before the onset of symptoms, it is possible that this interaction partly plays a causative role in the pathogenesis of ALS.

To test whether mutant SOD1 directly interacts with tubulin, we purified recombinant mutant SOD1 proteins with a His tag (Supplemental Fig. 1B). Purified α/β-tubulin from bovine brain (Supplemental Fig. 1B) and His-tagged SOD1 proteins were mixed and pull-down assays were performed. Tubulin was precipitated with apo mutant SOD1 (Fig. 2A), indicating that mutant SOD1 can directly interact with tubulin. Tubulin was also precipitated with apo wild-type SOD1 (Supplemental Fig. 2).

The mutant SOD1-binding site within tubulin partly overlaps with the binding site for nocodazole

To determine the mutant SOD1-binding region within tubulin, we performed pull-down assays using the tubulin-binding agents paclitaxel, noscapine and nocodazole. We found that nocodazole inhibited the interaction between mutant SOD1 and tubulin, while paclitaxel and noscapine did not (Fig. 2A–C). The nocodazole binding site overlaps with that for colchicine [9]. Colchicine also inhibited the interaction between mutant SOD1 and tubulin (data not shown). The paclitaxel binding site within tubulin is distinct from those for noscapine and colchicine [10,11]. Thus the mutant SOD1-binding region of tubulin in part overlaps with the region(s) bound by nocodazole and colchicine, but does not overlap with the regions bound by paclitaxel and noscapine.

Amino acid residues 1–23 and 116–153 of SOD1 interact with tubulin

We next assessed whether tubulin interacts with the C-terminal deletion mutant T116X SOD1, which has been reported to cause ALS-like phenotype in mice [12]. Coimmunoprecipitation assays using FLAG-tagged T116X SOD1 (Fig. 2D) revealed that mutant T116X SOD1 interacts with tubulin (Fig. 2E), indicating that tubulin interacts with amino acid residues 1–115 of mutant SOD1. Silver staining analysis also showed that, similarly to A4V SOD1, mutant T116X SOD1 interacts with multiple proteins (Fig. 2F). This indicates that interacting with various proteins is a common abnormal property shared by ALS-associated mutant SOD1 proteins. We observed that tubulin also interacts with amino acid residues 116–153 of SOD1 (Fig. 2G and H). To determine the tubulin-binding region within residues 1–115 of SOD1, we further performed coimmunoprecipitation assays using deletion mutants of SOD1 (Fig. 2I). We found that amino acid residues 11–115 and 1–85 of SOD1 interact with tubulin, while amino acid residues 24–115 and 38–115 do not (Fig. 2J). Moreover, amino acid residues 1–10 and 1–23 of SOD1 both interacted with tubulin (Fig. 2K and L). These results suggest that tubulin interacts with amino acid residues 1–23 and 116–153 of mutant SOD1.

Cys-111 of mutant SOD1 affects the interaction with tubulin

SOD1 contains four cysteine residues, Cys-6, 57, 111 and 146. Recent studies have shown that, among these cysteine residues, Cys-111 in particular affects the aggregation and cytotoxicity of mutant SOD1 [13]. The substitution of Cys-111 to serine (C111S) significantly inhibits the aggregation or cytotoxicity of mutant SOD1 [13].

To examine the correlation between the cytotoxicity of mutant SOD1 and the interaction of mutant SOD1 with tubulin, we performed coimmunoprecipitation assays using mutant SOD1 containing serine substitutions at each cysteine residue. Interestingly, immunoblotting analyses showed that the C111S substitution in mutant SOD1 significantly decreased the interaction between tubulin and mutant SOD1, although C6S, C57S and C146S substitutions did not (Fig. 3A and B). Together with the report showing the role of Cys-111 in cytotoxicity and aggregation of mutant SOD1 [13], our results suggest that the cytotoxicity of mutant SOD1 is correlated with the degree of its interaction with tubulin. Silver staining analyses also showed that the C111S substitution in mutant SOD1 decreased the interaction between multiple proteins and mutant SOD1 (~50% decrease), while C6S, C57S and C146S substitutions did not (Fig. 3C).

Overexpression of mutant SOD1 causes accumulation of tubulin in insoluble fractions

Given that mutant SOD1 physically interacts with tubulin, and that mutant SOD1 forms insoluble aggregates when overexpressed in cells, we hypothesized that mutant SOD1 causes aggregation of tubulin. To examine the effects of mutant SOD1 on the aggregation of tubulin, we prepared 1% Triton X-100-soluble and insoluble fractions from cells overexpressing wild-type or mutant SOD1, and the amount of tubulin in each fraction was analyzed. An increased level of SOD1 was detected in the insoluble fraction of cells overexpressing mutant SOD1 compared with that of cells

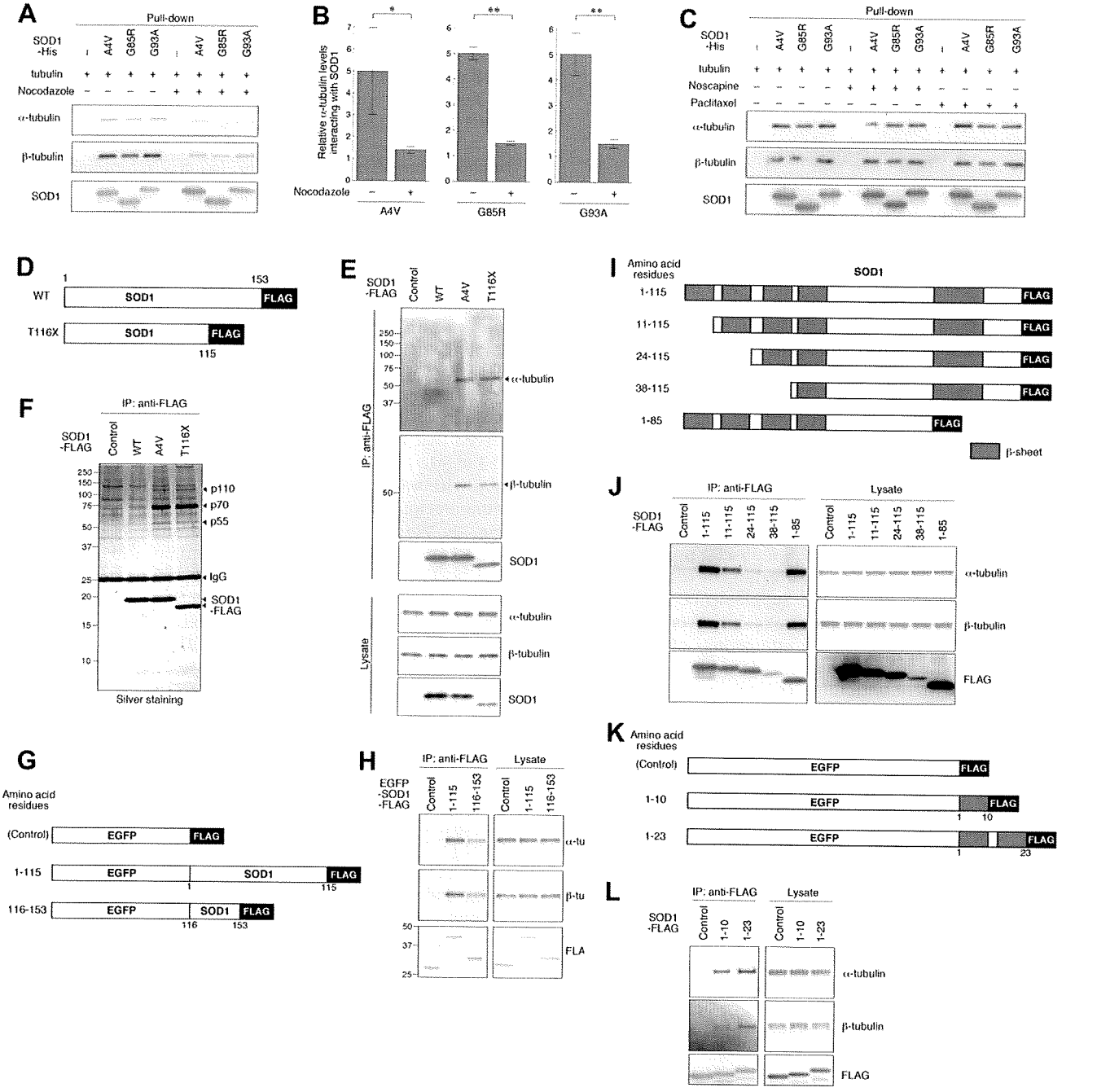

Fig. 2. Binding site within tubulin and mutant SOD1. (A–C) Forty micromolars of nocodazole (A), paclitaxel (C), noscapine (C) or vehicle was mixed with the indicated purified proteins and pull-down assays were performed. Precipitants were analyzed by immunoblotting. The relative levels of α-tubulin interacting with mutant SOD1 were quantified by densitometry. Mean values are shown with SD ($n = 3$). $^{*}p < 0.05$; $^{**}p < 0.01$ (B). (D, G, I, and K) Schematic representation of deletion mutants of SOD1. (E, F, H, J, and L) Lysates of COS-7 cells transfected with the indicated constructs were immunoprecipitated with an anti-FLAG antibody and analyzed by immunoblotting (E, H, J, and L) or silver staining (F).

overexpressing wild-type SOD1 (Fig. 3D) We found that overexpression of mutant SOD1 resulted in increased levels of α- and β-tubulin in the insoluble fraction, but had no effect on the protein levels in the soluble fraction (Fig. 3D and E). By contrast, overexpression of wild-type SOD1 did not alter the levels of α- and β-tubulin in either fraction (Fig. 3D and E). In both fractions, the level of β-actin, which does not interact with mutant SOD1 (Fig. 1C), was not affected by the overexpression of wild-type or mutant SOD1 (Fig. 3D). These results indicate that the accumulation of tubulin in insoluble fractions is mediated by the interaction between mutant SOD1 and tubulin. Since the insoluble aggregates associated with neurodegenerative diseases exhibit protease resistance [14], it is possible that aggregated tubulin exhibits resistance to constitutive degradation, resulting in the accumulation of insoluble tubulin in cells overexpressing mutant SOD1.

Mutant SOD1 directly modulates tubulin polymerization

To elucidate the direct effect of mutant SOD1 on microtubule dynamics, we used a cell-free tubulin polymerization assay. We confirmed that paclitaxel, a microtubule-stabilizing agent, promotes tubulin polymerization, and that nocodazole, a microtu-

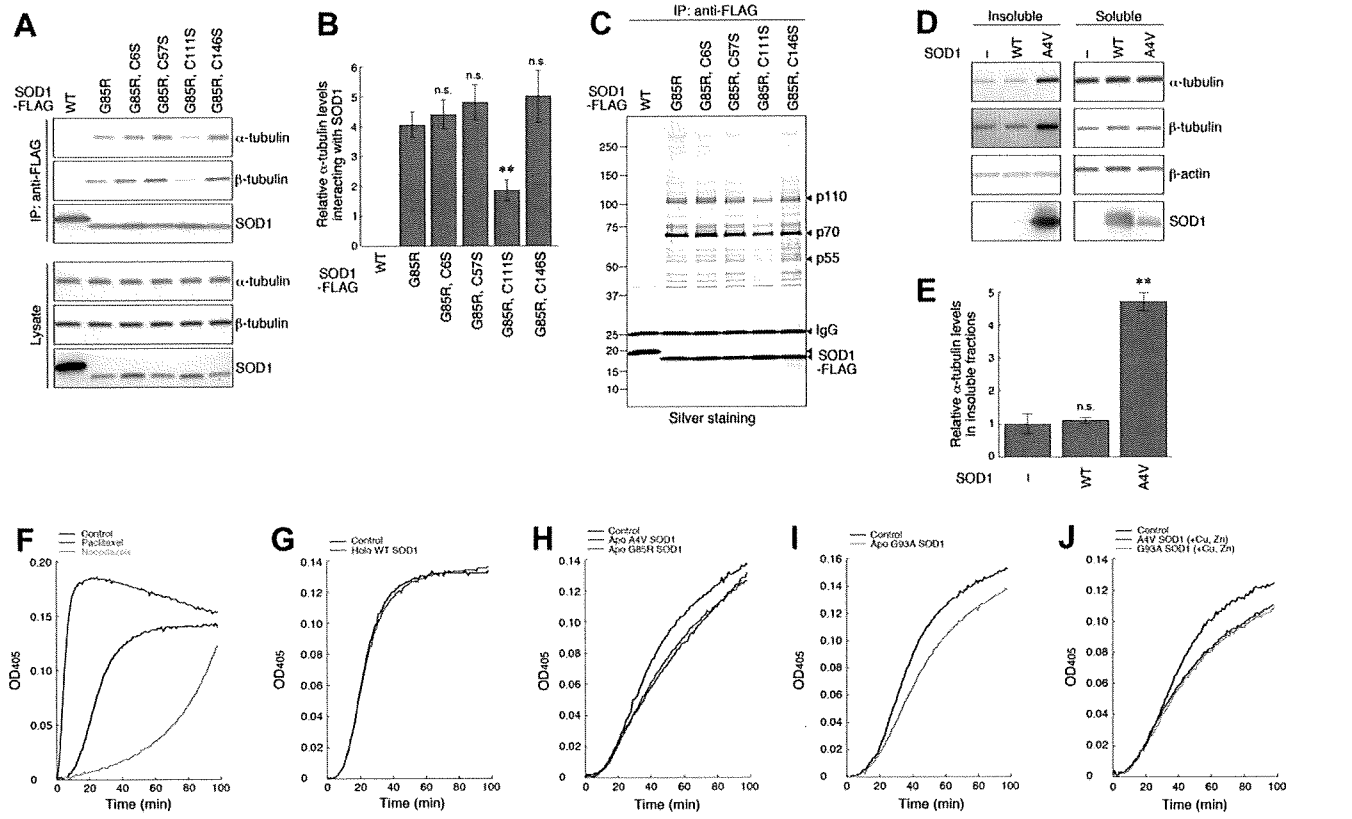

Fig. 3. Effects of mutant SOD1 on tubulin. (A–C) Lysates of Neuro2a cells transfected with the indicated constructs were immunoprecipitated with anti-FLAG antibody and analyzed by immunoblotting (A) or silver staining (C). The relative levels of α-tubulin interacting with mutant SOD1 were quantified by densitometry (B). Mean values are shown with SD ($n = 3$). n.s., not significant; $^{**}p < 0.01$ (B, Dunnett's multiple comparison test). (D,E) pEF-hSOD1 (WT or A4V) or empty vector was transfected into COS-7 cells. Three days after transfection, soluble and insoluble fractions were prepared and analyzed by immunoblotting (D). The relative levels of α-tubulin in the insoluble fractions were quantified by densitometry. Mean values are shown with SD ($n = 3$). n.s., not significant; $^{**}p < 0.01$ (E, Dunnett's multiple comparison test). (F) A tubulin polymerization assay was performed in the presence of 10 μM paclitaxel, 10 μM nocodazole or vehicle (control, DMSO). Light scattering was used to measure the amount of polymerized microtubules. (G–J) Four microliters of 1 μg/μl holo wild-type SOD1 or vehicle (200 μM $CuSO_4$, 200 μM $ZnCl_2$ in 20 mM sodium phosphate buffer, pH 8.0) was mixed with 100 μl of 3 mg/ml tubulin (G). Twenty microliters of 0.2 μg/μl apo mutant SOD1 or vehicle (20 mM sodium phosphate buffer, pH 8.0) was mixed with 80 μl of 3.75 mg/ml tubulin (H,I). Twenty microliters of 0.2 μg/μl holo mutant SOD1 or vehicle (200 μM $CuSO_4$, 200 μM $ZnCl_2$ in 20 mM sodium phosphate buffer, pH 8.0) was mixed with 80 μl of 3.75 mg/ml tubulin (J). Then tubulin polymerization assays were performed. The assays were performed at least three times; representative results are shown. Wild-type SOD1 did not inhibit tubulin polymerization when we used 20 μl of 0.2 μg/μl holo wild-type SOD1 (data not shown).

bule-destabilizing agent inhibits tubulin polymerization in a cell-free system (Fig. 3F). We prepared wild-type and mutant SOD1 proteins without a tag (Supplemental Fig. 1C and Supplemental Table 1), and performed tubulin polymerization assays. Because apo wild-type SOD1 interacts with tubulin, we used holo wild-type SOD1 as a control native SOD1. Wild-type SOD1 had almost no effect on tubulin polymerization (Fig. 3G). Interestingly, mutant SOD1 inhibited tubulin polymerization in tubulin polymerization assays (Fig. 3H–J). These results are consistent with the results showing that tubulin interacts with mutant SOD1, but not with wild-type SOD1, and indicate that mutant SOD1 directly affects the stability of microtubules.

Discussion

The microtubule-destabilizing agent colchicine has been reported to induce neuronal cell death in mice [15]. Microtubule-stabilizing agents such as paclitaxel are effective chemotherapeutic agents for the treatment of many cancers. However, neuropathy is a major adverse effect of microtubule-stabilizing agent-based chemotherapy [16]. Paclitaxel is also reported to induce cell death in cortical neurons [17]. Thus tightly regulated microtubule dynamics, namely controlled tubulin polymerization/depolymerization, are required for neurons to remain viable, and our results may indicate that the physical interaction of mutant SOD1 with α/β-tubulin at least partly underlies the neurodegeneration mediated by mutant SOD1.

A recent report has shown that microtubule dynamics are increased in the motor neurons of mutant G93A SOD1 transgenic mice, and that this increase in microtubule dynamics in motor neurons is associated with altered axonal transport and motor neuron degeneration [18]. We have shown that mutant SOD1 directly interacts with tubulin (Fig. 2A), and that mutant SOD1 has a similar effect on microtubules to a microtubule-destabilizing agent, but to a lesser extent (Fig. 3F–J). Since microtubules in neurons are relatively stable due to their interactions with microtubule-associated proteins, destabilization of microtubules may cause increased microtubule dynamics in neurons. Taken together, our results suggest that mutant SOD1 can directly increase microtubule dynamics through its destabilizing effect on microtubules in neurons.

Using tubulin-binding agents, we have shown that the mutant SOD1-binding site within tubulin in part overlaps with the sites bound by colchicine and nocodazole (Fig. 2A–C). Considering that colchicine destabilizes microtubules through the interaction with tubulin at microtubule ends [19], mutant SOD1 may also modulate microtubule dynamics through the interaction with tubulin at microtubule ends. Structural analysis of the interaction of SOD1 with tubulin, such as X-ray crystallography, is required for further understanding of the mechanism that underlies the modulation of microtubule dynamics by mutant SOD1. Native SOD1 forms a sta-

ble homodimer, while mutant SOD1 partly exists as a monomer [20]. We showed that amino acid residues 1–23 and 116–153 in SOD1 interact with tubulin (Fig. 2D–L). These amino acid residues contain residues 4–8 and 143–151, which are sequestered in the SOD1 dimer interface and are inaccessible in native SOD1 [20]. We also showed that tubulin interacts with apo wild-type SOD1 (Supplemental Fig. 2). Apo SOD1 has been reported to exist substantially as a monomer [8]. Together, our results suggest that tubulin interacts with monomeric SOD1. The inhibitory effects of holo mutant SOD1 on tubulin polymerization (Fig. 3J) may be due to the misfolded or remaining apo SOD1 in the recombinant SOD1 sample, considering that the enzymatic activities of holo mutant SOD1 were reduced compared with that of wild-type SOD1 (Supplemental Table 1).

In addition to tubulin, we observed that SOD1 mutants specifically interact with multiple proteins (Fig. 1A and B and 3C). The C111S substitution in mutant SOD1 decreases the degree of interaction between mutant SOD1 and various proteins (Fig. 3C), suggesting that most mutant SOD1-interacting proteins bind to SOD1 in a similar way. These other interactors may also be involved in the mechanism underlying SOD1-mediated neurodegeneration. We have identified some of these interactors, and these proteins are currently under investigation.

Our present study demonstrates that mutant SOD1 can directly modulates tubulin polymerization by physically interacting with tubulin. The findings in the present study provide novel insights into the mechanisms underlying the pathology of ALS.

Acknowledgments

We thank Dr. Ryosuke Takahashi (Kyoto University) and Dr. Makoto Urushitani (Shiga University of Medical Science) for the gift of pcDNA3-hSOD1-FLAG plasmids. We also thank Dr. H. Akiko Popiel (National Institute of Neuroscience) for support with English. This work was supported by Grants-in-Aid for Scientific Research of Japan Society for the Promotion of Science; Research Grant in Priority Area Research of the Ministry of Education, Culture, Sports, Science and Technology, Japan; Grants-in-Aid for Scientific Research of the Ministry of Health, Labour and Welfare, Japan and the Program for Promotion of Fundamental Studies in Health Sciences of the National Institute of Biomedical Innovation, Japan.

Appendix A. Supplementary data

Supplementary data associated with this article can be found, in the online version, at doi:10.1016/j.bbrc.2009.06.138.

References

[1] M.E. Gurney, H. Pu, A.Y. Chiu, M.C. Dal Canto, C.Y. Polchow, D.D. Alexander, J. Caliendo, A. Hentati, Y.W. Kwon, H.X. Deng, W. Chen, P. Zhai, R.L. Sufit, T. Siddique, Motor neuron degeneration in mice that express a human Cu,Zn superoxide dismutase mutation, Science 264 (1994) 1772–1775.

[2] A.G. Reaume, J.L. Elliott, E.K. Hoffman, N.W. Kowall, R.J. Ferrante, D.F. Siwek, H.M. Wilcox, D.G. Flood, M.F. Beal, R.H. Brown Jr., R.W. Scott, W.D. Snider, Motor neurons in Cu/Zn superoxide dismutase-deficient mice develop normally but exhibit enhanced cell death after axonal injury, Nat. Genet. 13 (1996) 43–47.

[3] H. Nishitoh, H. Kadowaki, A. Nagai, T. Maruyama, T. Yokota, H. Fukutomi, T. Noguchi, A. Matsuzawa, K. Takeda, H. Ichijo, ALS-linked mutant SOD1 induces ER stress- and ASK1-dependent motor neuron death by targeting Derlin-1, Genes Dev. 22 (2008) 1451–1464.

[4] T. Kabuta, R. Setsuie, T. Mitsui, A. Kinugawa, M. Sakurai, S. Aoki, K. Uchida, K. Wada, Aberrant molecular properties shared by familial Parkinson's disease-associated mutant UCH-L1 and carbonyl-modified UCH-L1, Hum. Mol. Genet. 17 (2008) 1482–1496.

[5] T. Kabuta, A. Furuta, S. Aoki, K. Furuta, K. Wada, Aberrant interaction between Parkinson disease-associated mutant UCH-L1 and the lysosomal receptor for chaperone-mediated autophagy, J. Biol. Chem. 283 (2008) 23731–23738.

[6] T. Kabuta, Y. Suzuki, K. Wada, Degradation of amyotrophic lateral sclerosis-linked mutant Cu, Zn-superoxide dismutase proteins by macroautophagy and the proteasome, J. Biol. Chem. 281 (2006) 30524–30533.

[7] H. Yamashita, J. Kawamata, K. Okawa, R. Kanki, T. Nakamizo, T. Hatayama, K. Yamanaka, R. Takahashi, S. Shimohama, Heat-shock protein 105 interacts with and suppresses aggregation of mutant Cu/Zn superoxide dismutase: clues to a possible strategy for treating ALS, J. Neurochem. 102 (2007) 1497–1505.

[8] M. Urushitani, J. Kurisu, M. Tateno, S. Hatakeyama, K. Nakayama, S. Kato, R. Takahashi, CHIP promotes proteasomal degradation of familial ALS-linked mutant SOD1 by ubiquitinating Hsp/Hsc70, J. Neurochem. 90 (2004) 231–244.

[9] J. Hoebeke, G. Van Nijen, M. De Brabander, Interaction of oncodazole (R 17934), a new antitumoral drug, with rat brain tubulin, Biochem. Biophys. Res. Commun. 69 (1976) 319–324.

[10] J. Zhou, K. Gupta, J. Yao, K. Ye, D. Panda, P. Giannakakou, H.C. Joshi, Paclitaxel-resistant human ovarian cancer cells undergo c-Jun NH_2-terminal kinase-mediated apoptosis in response to noscapine, J. Biol. Chem. 277 (2002) 39777–39785.

[11] R.B. Ravelli, B. Gigant, P.A. Curmi, I. Jourdain, S. Lachkar, A. Sobel, M. Knossow, Insight into tubulin regulation from a complex with colchicine and a stathmin-like domain, Nature 428 (2004) 198–202.

[12] D. Han-Xiang, J. Hujun, F. Ronggen, Z. Hong, S. Yong, L. Erdong, H. Makito, C.D. Mauro, S. Teepu, Molecular dissection of ALS-associated toxicity of SOD1 in transgenic mice using an exon-fusion approach, Hum. Mol. Genet. 17 (2008) 2310–2319.

[13] M. Cozzolino, I. Amori, M.G. Pesaresi, A. Ferri, M. Nencini, M.T. Carri, Cysteine 111 affects aggregation and cytotoxicity of mutant Cu, Zn-superoxide dismutase associated with familial amyotrophic lateral sclerosis, J. Biol. Chem. 283 (2008) 866–874.

[14] R.M. Murphy, Peptide aggregation in neurodegenerative disease, Annu. Rev. Biomed. Eng. 4 (2002) 155–174.

[15] Y. Liang, S. Li, C. Wen, Y. Zhang, Q. Guo, H. Wang, B. Su, Intrastriatal injection of colchicine induces striatonigral degeneration in mice, J. Neurochem. 106 (2008) 1815–1827.

[16] J.J. Lee, S.M. Swain, Peripheral neuropathy induced by microtubule-stabilizing agents, J. Clin. Oncol. 24 (2006) 1633–1642.

[17] X.A. Figueroa-Masot, M. Hetman, M.J. Higgins, N. Kokot, Z. Xia, Taxol induces apoptosis in cortical neurons by a mechanism independent of Bcl-2 phosphorylation, J. Neurosci. 21 (2001) 4657–4667.

[18] P. Fanara, J. Banerjee, R.V. Hueck, M.R. Harper, M. Awada, H. Turner, K.H. Husted, R. Brandt, M.K. Hellerstein, Stabilization of hyperdynamic microtubules is neuroprotective in amyotrophic lateral sclerosis, J. Biol. Chem. 282 (2007) 23465–23472.

[19] R.L. Margolis, L. Wilson, Addition of colchicine–tubulin complex to microtubule ends: the mechanism of substoichiometric colchicine poisoning, Proc. Natl. Acad. Sci. USA 74 (1977) 3466–3470.

[20] R. Rakhit, J. Robertson, C. Vande Velde, P. Horne, D.M. Ruth, J. Griffin, D.W. Cleveland, N.R. Cashman, A. Chakrabartty, An immunological epitope selective for pathological monomer-misfolded SOD1 in ALS, Nat. Med. 13 (2007) 754–759.

Neurochemistry International 54 (2009) 314–321

Contents lists available at ScienceDirect

Neurochemistry International

journal homepage: www.elsevier.com/locate/neuint

Ubiquitin dimers control the hydrolase activity of UCH-L3

Rieko Setsuie [a], Mikako Sakurai [a,1], Yuriko Sakaguchi [b], Keiji Wada [a,*]

[a] Department of Degenerative Neurological Diseases, National Institute of Neuroscience, National Center of Neurology and Psychiatry, 4-1-1 Ogawahigashi, Kodaira, Tokyo 187-8502, Japan
[b] Department of Chemistry and Biotechnology, Graduate School of Engineering, The University of Tokyo, Bunkyo-ku, Tokyo, Japan

ARTICLE INFO

Article history:
Received 29 September 2008
Received in revised form 3 December 2008
Accepted 15 December 2008
Available online 25 December 2008

Keywords:
Ubiquitin
Ubiquitin dimer
Ubiquitin carboxy terminal hydrolase-L1 (UCH-L1)
Ubiquitin carboxy terminal hydrolase-L3 (UCH-L3)

ABSTRACT

Ubiquitin (Ub) carboxy terminal hydrolase (UCH)-L1 and UCH-L3 are two of the deubiquitinating enzymes expressed in the brain. Both *gad* mice, which lack UCH-L1 expression and *Uchl3* knockout mice exhibit neurodegeneration, although at distinct areas. These phenotypes indicate the importance of UCH-L1 and UCH-L3 in the regulation of the central nervous system. However, molecular substrates and the molecular regulators of UCH-L1 and UCH-L3 remain poorly identified. Here we show that Ub dimers interact non-covalently with UCH-L3 *in vitro* and in cells. These interactions were not observed with UCH-L1 in cells. *In vitro*, K48-linked Ub dimers pronouncedly inhibited the hydrolase activity of UCH-L3, while mono-Ub, a previously identified interacting protein, inhibited the hydrolase activity of UCH-L1. These results indicate that mono-Ub and Ub dimers may regulate the enzymatic functions of UCH-L1 and UCH-L3, respectively, *in vivo*.

1. Introduction

The ubiquitin (Ub) system is involved in the regulation of various physiological phenomena including development, inflammatory response, and intracellular trafficking (Hershko and Ciechanover, 1998; Hicke, 2001; Glickman and Ciechanover, 2002; Mukhopadhyay and Riezman, 2007). Malfunction of the Ub system in the central nervous system (CNS) may lead to neurodegeneration or synaptic dysfunction (Rubinsztein, 2006; Hegde and Upadhya, 2007). Ub can be covalently conjugated to substrate proteins by the sequential action of E1, E2 and E3 enzymes forming an isopeptide bond between the carboxy terminus of Ub and the lysine residues of the substrates (Hershko and Ciechanover, 1998). The attachment of Ub to the substrates may occur either in the form of a single Ub or a poly-Ub chain, where the carboxy terminus of one Ub moiety is covalently linked to one of the seven Lys residues of an adjacent Ub molecule.

Deubiquitination involves the hydrolysis of the isopeptide bonds between the carboxy terminus glycine of the Ub and the lysine of the substrates or Ub, which requires the activity of deubiquitinating enzymes (DUBs) (Nijman et al., 2005). DUBs can be divided into six distinct families: the Ub-specific processing proteases, the Ub carboxyl-terminal hydrolases (UCHs), the Ataxin-3/Josephin domains, the ovarian tumor domain-containing proteases, the viral processing proteases and the JAMM proteases.

UCH is a cysteine protease with relatively small molecular weight. There is one UCH in yeast, and four UCH isozymes in mammals: UCH-L1, UCH-L3, UCH37 and BAP1. Of these, UCH-L1 and UCH-L3 are the most closely related family members with about 53% identity. These UCHs have also been shown to hydrolyze Nedd8 (neural precursor cell expressed developmentally down regulated 8), a Ub-like protein with 68% identity to Ub (Wada et al., 1998; Hemelaar et al., 2004). The expression of UCH-L3 is ubiquitous whereas that of UCH-L1 is mainly restricted to the brain and the testis/ovary (Wilkinson et al., 1989; Kurihara et al., 2000; Kurihara et al., 2001).

Previous studies using mutant mice of *Uchl1* and *Uchl3* indicated that these enzymes are involved in the regulation of the brain function (Setsuie and Wada, 2007). The I93M point mutation in UCH-L1 is associated with familial Parkinson's disease (Leroy et al., 1998) and we have previously shown that I93M UCH-L1 expression in the cell or in transgenic mice induces dopaminergic neuron death (Setsuie et al., 2007; Kabuta et al., 2008). We also reported that *gad* (gracile axonal dystrophy) mice, which lack Uchl1 expression, show axonal degeneration of the gracile tract, which results in sensory ataxia (Saigoh et al., 1999). Our analysis also indicated that UCH-L1 is involved in many biological aspects including neuronal apoptosis (Harada et al., 2004), neurotransmitter receptor activation (Manago et al., 2005), neural progenitor regulation (Sakurai et al., 2006), learning and memory (Sakurai et al., 2008). On the other hand, UCH-L3 knockout mice show photoreceptor cell degeneration (Semenova

* Corresponding author. Tel.: +81 42 346 1715; fax: +81 42 346 1745.
E-mail address: wada@ncnp.go.jp (K. Wada).
[1] Present address: Department of Pathology and Taub Institute, Columbia University, New York, NY 10032, USA.

0197-0186/$ – see front matter © 2008 Elsevier Ltd. All rights reserved.
doi:10.1016/j.neuint.2008.12.013

et al., 2003; Sano et al., 2006) and defects in memory function (Wood et al., 2005). These different phenotypes of mutant mice indicate that although both enzymes share similar properties in terms of biochemical identity (Johnston et al., 1997; Larsen et al., 1998; Misaghi et al., 2005; Das et al., 2006), UCH-L1 and UCH-L3 should be differentially controlled or be regulated by distinct molecules.

To identify the proteins that regulate UCH-L1 and UCH-L3 in a diverse manner, we performed immunoaffinity purification assay using UCH-L1 and UCH-L3 and found that UCH-L3 is inhibited by Ub dimers (di-Ub) while UCH-L1 is inhibited by mono-Ub.

2. Experimental procedures

2.1. Isolation and culture of mouse embryonic fibroblasts (MEFs) and their immortalization

Pregnant female *Uchl3* heterozygote mice (Kurihara et al., 2000) were sacrificed at 14–15 days postcoitus. The head, the viscera and the bones of each embryo were removed under a dissecting microscope and a part of these samples were used for genotyping. The remaining portion of embryo was placed in 0.25% trypsin-EDTA (Invitrogen, Carlsbad, CA, USA), cut finely with razor blade, and incubated for 15 min at 37 °C. The cell suspension was passed several times through a 1 ml pipette tip until no clumps were visible. The cell suspension prepared from each individual embryo was washed with medium containing 10% (v/v) fetal bovine serum (FBS). Viable cells were determined by trypan-blue exclusion assay and 4,000,000 viable cells from each embryo were plated in 100 mm culture dishes. MEFs were maintained in Dulbecco's Modified Eagle's Medium (Sigma, St. Louis, MO, USA) supplemented with 10% (v/v) FBS (JRH, Biosciences, Lenexa, KS, USA), 100 U/ml penicillin and streptomycin (Invitrogen). The genotype was determined using the remnants of tissues, and polymerase chain reactions (PCR) were conducted using the primers and the thermal cycling as follows: L3KO-1 primer (5′-ggaactactgagccatatgtgc-3′) L3KO-2 primer (5′-cggacttactccatcacttcac-3′) L3KO-3 primer (5′-cttgtgagcgccaagtgc-3′), one cycle of 98 °C for 5 min, 30 cycles at 98 °C for 10 s, 60 °C for 20 s, and 72 °C for 30 s. For the immortalization of MEFs, basic 3T3 protocols were carried out as described (Todaro and Green, 1963).

2.2. Construction of cell lines expressing human wild-type or mutant UCH-L3

Retrovirus vectors encoding human wild-type UCH-L3 were constructed as follows. Full-length human UCH-L3 cDNA was cloned from human liver cDNA library and inserted into the pGEM-T vector (Promega, Madison, WI, USA). For PCR-based amplification of the insert, the huchl3-retro-s2 primer (5′-GGGGCTCGAGCGCGG-CATGGAGGGTCAACGCTGGCT-3′) and huchl3-pci-as1 primer (5′-GGGGGCGGCC-GCCTATGCTGCAGAAAGAGC AATCG-3′) were used with 35 cycles of 94 °C for 30 s, 55 °C for 30 s and 72 °C for 1 min. The amplified PCR fragment and pOZ-N retrovirus vector were successively digested with XhoI and NotI. The enzymatically digested PCR fragment and pOZ-N vector were subsequently applied to electrophoresis, gel extraction and ligated using the ligation system ver2 (Takara, Tokyo, Japan). This resulted in the insertion of human UCH-L3 without a starting methionine after the HA and FLAG double-tag sequence between the XhoI and NotI sites at the multicloning site of the pOZ-N double-tag retrovirus vector. To obtain Ub hydrolase-deficient C95S mutant- and Ub affinity deficient D33A mutant-encoding retrovirus vectors, the Cys95 or Asp33 of hUCH-L3 were mutated to Ser or Ala, respectively, using PCR-based *in vitro* mutagenesis (Stratagene, La Jolla, CA, USA). The primers used for mutagenesis were huchl3-C95S-s1 (5′-ATCAGCAATGCAATGCCTGTGGAAC AATTGGA-3′), hchl3-C95S-as1 (5′-TCCAATTGTTCCACAGGCATTGCTGAT-3′), huchl3-D33A-s (5′-CTAACT-GGCAATTCGTTGCTGTATATGGAATGGATCC TGAAC-3′) and huchl3-D33A-as (5′-GTTCAGGATCCATTCCATATA CAGCAACGAATTGCCAGTTAG-3′). The human UHCL1 or GFP cDNA derived inserts were cloned into the XhoI and NotI site of the same retrovirus vector, as described previously (Sakurai et al., 2006). The production of retroviruses and cell lines were conducted as described elsewhere (Ogawa et al., 2002).

2.3. Immunoprecipitation

2.5×10^8 floating Hela cells expressing FLAG-HA tagged hUCH-L3 were collected and washed with phosphate buffered saline (PBS) twice and the cell pellets were stored at −80 °C until all of the clones were ready for lysis. The floating Hela cells were quickly thawed at 37 °C, suspended in 15 ml of ice-cold modified RIPA buffer (50 mM Tris–HCl (pH 7.4), 1% Nonidet P40, 0.25% sodium deoxycholate, 150 mM NaCl, 1 mM EDTA, 1 mM $NaVO_4$, 1 mM NaF with Complete EDTA-free protease inhibitors (Roche Diagnostics, Indianapolis, IN, USA)), and kept on ice for 30 min. After three repeated sonications for 10 s with 30 s intervals, lysates were centrifuged at 12,000 rpm at 4 °C for 10 min using a swing-rotor type centrifuge. The supernatant was recovered for further purification and aliquots were kept at −80 °C as a pre-immunoprecipitation lysate. To the remaining supernatant, anti-FLAG M2 antibody-conjugated agarose (Sigma) in 600 μl slurry was added and gently rotated at 4 °C for 8 h. After rotation, the samples were poured into the empty column (Bio-Rad, Hercules, CA, USA), washed four times with 8 ml 0.1 B buffer (20 mM Tris–HCl (pH 8.0), 0.1 M KCl, 5 mM $MgCl_2$, 10% glycerol, 0.1% Tween-20, 10 mM β-mercaptoethanol, 0.2 mM PMSF), and briefly centrifuged to remove the excess washing buffer. After capping the bottom of the column, 600 μl elution buffer (160 μg/ml of 3× FLAG peptide in 0.1 B buffer) were added to the column, rotated at 4 °C for 1 h, and eluted into an eppendorf tube. This elution step was repeated and a total of 1.2 ml eluate was used for the second purification. The second purification was performed using the anti-HA antibody (clone 12CA5)-conjugated agarose. The steps were the same as for FLAG purification except that the scale was minimized with 100 μl of elution (1 mg/ml HA peptide (Roche) in 0.1 B buffer). The resulting final eluates were kept at −80 °C until analysis.

2.4. Mass spectrometry analysis

After the negative staining (Nakalai Tesque Inc., Kyoto, Japan) of the SDS-PAGE gels, protein bands were sliced from the gel, reduced, S-alkylated, and subjected to in-gel trypsin digestion. The digested peptides were extracted with 50% acetonitrile and 0.1% trifluoroacetic acid and subjected to liquid-chromatography tandem mass spectrometry (LC–MS/MS) analysis.

2.5. Silver staining and Western blotting

Silver staining was done using the Daiichi Silver staining Kit (Daiichi, Tokyo, Japan). For the Western blotting of UCH-L3 or HA-FLAG tagged UCH-L3, 15% mini gels (DRC, Tokyo, Japan) were used. For the detection of mono- or di-Ub, or Nedd8, 15–20% gradient mini gels (DRC) were used. For 2D-Western blotting, samples were loaded on 4–11 N IPG strips (GE Healthcare UK Ltd., Buckinghamshire, England) using IPGphor and the second dimension was run on 15–20% gradient gels (DRC). The antibodies used were anti-HA antibody (clone 12CA5, 1:1,000), anti-FLAG M2 antibody (Sigma; 1:1000), anti-Ub antibody (Sigma; 1:1000 or Dako; 1:1000), anti-Nedd8 antibody (Cell signaling; 1:1000) anti-UCH-L1 antibody (Ultraclone RA95101; 1:5000, England, UK) and anti-UCH-L3 antibody ((Kwon et al., 2004); 1:1,000). HRP-conjugated secondary antibodies were from Pierce and signals were detected using a chemiluminescent Super Signal West Dura Extended Duration Substrate kit or West Femto Maximum Sensitivity Substrate kit (Pierce, Rochford, IL) and analyzed with a ChemiImager (Alpha Innotech, San Leandro, CA). The protein marker was purchased from Bio-Rad.

2.6. Pull-down assay

6HN-tagged human UCH-L3 and UCH-L1 proteins were prepared as described previously (Nishikawa et al., 2003). Pull-down assay was conducted as described previously with some modifications (Kabuta et al., 2008). In brief, 6 μg 6HN-UCH and 4 μg of either K48-linked di-Ub, K63-linked di-Ub, or linear di-Ub (all from Boston Biochem, Cambrige, MA, USA), were mixed in the presence of 0.1 μg/ml BSA in tris-buffered saline (TBS) at 4 °C for 2 h. Fifty micro liters of TALON resin (Clontech, Palo Alto, CA, USA) were added to samples and incubated at 4 °C for 1 h. After washing the resin five times with PBS in the presence of 20 mM imidazole and 0.05% Tween-20, the bound proteins were eluted with SDS sample buffer.

2.7. Ubiquitin hydrolase activity assay

The Ub hydrolase activity assay, using recombinant UCH-L3 and Ub-AMC (both from Boston Biochem), was performed as described previously (Nishikawa et al., 2003), in the presence or absence of di-Ub.

3. Results

3.1. UCH-L3 but not UCH-L1 interacts with di-Ub

To identify the proteins that interact with UCH-L1 or UCH-L3, which might represent the potential substrates or the functional effecters, we performed immunoaffinity chromatography. Floating Hela cells that stably expressed human UCH-L3 tagged with the FLAG-HA epitope at its N-terminus (L3 WT), UCH-L3 C95S (active site mutant of UCH-L3), UCH-L1 (L1 WT), UCH-L1 C90S (active site mutant of UCH-L1), GFP and Mock were constructed (Fig. 1A). Western blotting using anti-HA and anti-FLAG antibodies detected a single band at the appropriate molecular weight in each cell line indicating FLAG-HA tagged proteins were sufficiently expressed and at comparable levels (Fig. 1A). We detected two bands with the anti-UCH-L3 antibody in all of the cell lines; these bands correspond to the exogenously expressed and endogenously expressed UCH-L3 in Hela cells (Fig. 1A).

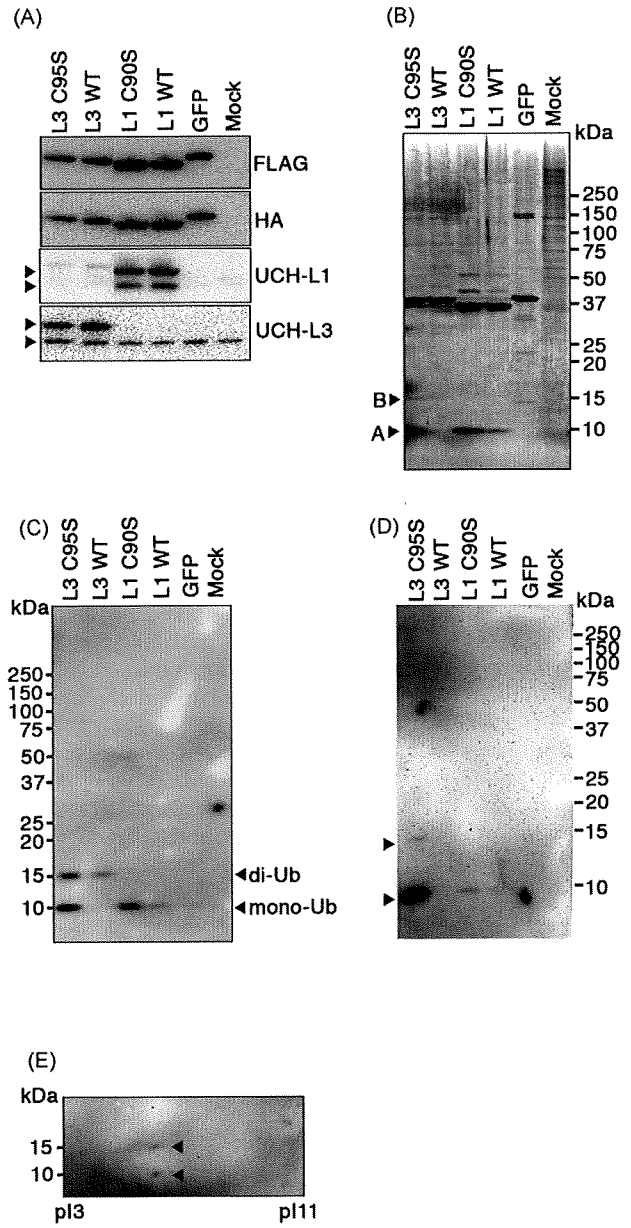

Fig. 1. Di-Ub interacts with UCH-L3. (A) Floating Hela cells stably expressing FLAG-HA double-tagged UCH-L3 or UCH-L1 were constructed. The expression of exogenous UCH-L3 or UCH-L1 was confirmed by anti-FLAG, anti-HA, anti-UCH-L1 and anti-UCH-L3 antibodies. Anti-UCH-L1 antibody showed two bands (indicated by the arrows), where upper band corresponds to the predicted molecular weight of UCH-L1 including FLAG-HA tag at the N-terminal. The lower band may indicate the N-terminally processed form of UCH-L1, which lack FLAG-HA tag. Anti-UCH-L3 antibody also showed two bands, where lower band represent the endogenous UCH-L3 expressed in Hela cells. (B) Silver staining of proteins, which are obtained by the sequential immunoaffinity purification using anti-FLAG antibody-conjugated agarose and anti-HA antibody-conjugated agarose. The bands, which are indicated by the arrow A and B were excised and processed for LC–MS/MS analysis. (C) Western blotting of the proteins as in (B) with anti-Ub antibody from Sigma–Aldrich. Note the presence of anti-Ub antibody immunoreactive bands at about 10 kDa and 15 kDa, which represent mono- and di-Ub. (D) Western blotting of the proteins as in (B) with anti-Nedd8 antibody from Cell Signaling. Note the presence of anti-Nedd8 antibody immunoreactive bands at about 10 kDa and 15 kDa, which may represent mono- and di-Nedd8. (E) 2D-Western blotting of the proteins, which is obtained by the sequential immunoaffinity purification of UCH-L3 C95S expressing Hela cell lysate as in (B). Anti-Ub antibody from Sigma–Aldrich is used.

UCH-L1- or UCH-L3-containing complexes were affinity purified from stable cells using anti-FLAG antibody-conjugated agarose, followed by anti-HA antibody-conjugated agarose and each elution was conducted under native conditions using 3×

Table 1
The amino acid sequences of fragments detected by the mass spectrometric analysis of bands A and B from Fig. 1B.

Band	Amino acid sequences
A	MQIFVKTLTG KTITLEVEPS DTIENVKAKI QDKEGIPPDQ QRLIFAGKQL EDGRTLSDYN IQKESTLHLV LRLRGG
B	MQIFVKTLTG KTITLEVEPS DTIENVKAKI QDKEGIPPDQ QRLIFAGKQL EDGRTLSDYN IQKESTLHLV LRLRGG

The bands, from the immunoaffinity-purified complex of C95S mutant corresponding to A and B of Fig. 1B, are excised and subjected to LC–MS/MS analysis as described in the Section 2, and the amino acid sequences in red are detected fragments by LC–MS/MS analysis.

FLAG peptide or HA peptide. After the second immunoaffinity chromatography, proteins associated with UCH-L3 WT, UCH-L3 C95S, UCH-L1 WT and UCH-L1 C90S were identified by SDS-PAGE followed by silver staining (Fig. 1B). The deduced amino acid sequences, which were obtained from the LC–MS/MS analysis, indicate that the bands with a molecular weight of about 9 kDa (arrow A) in Fig. 1B correspond to the free mono-Ub (Table 1). Consistently, the immunoblotting of immunoaffinity-purified proteins with anti-Ub antibody, which recognizes both free Ub and ubiquitylated proteins, revealed that these bands represent free mono-Ub (Fig. 1C). The finding that UCH-L1 and the UCH-L1 C90S mutant have strong affinity for mono-Ub is consistent with our previous finding that UCH-L1 interacts with and stabilizes free mono-Ub *in vivo* (Osaka et al., 2003). The strong detection of mono-Ub with the UCH-L3 C95S mutant complex but not with the UCH-L3 WT complex indicates that C95S mutation leads to either the conformational change resulting in the strong interaction with mono-Ub, or the lack of hydrolase activity that results in the interaction with the substrate.

The molecule with molecular weight of about 15 kDa (arrow B in Fig. 1B) identified for the UCH-L3 WT and UCH-L3 C95S immunoaffinity-purified proteins, and which had Ub sequence within this molecule, was of interest because this molecule was specific to UCH-L3 and not UCH-L1. Although the molecular weight is greater than for free mono-Ub, LC–MS/MS analysis of this band only revealed Ub (Table 1). It is known that free di-Ub has a size of about 15 kDa. To confirm whether the bands at 15 kDa (arrow B in Fig. 1B) are, in fact, free di-Ub, we performed 2D-Western blotting of the C95S immunoaffinity-purified complex using the anti-Ub antibody. The p*I* of di-Ub should be similar to that of mono-Ub. As shown in Fig. 1E, the 15 kDa molecule (upper arrow in Fig. 1E) had a p*I* similar to that of free mono-Ub (lower arrow in Fig. 1E), indicating that the band may represent di-Ub.

To confirm the direct interaction of di-Ub and UCH-L3, we performed pull-down assays using recombinant mono-Ub or di-Ub and UCH-L3. As shown in Fig. 2B, UCH-L3 can form physiological complexes not only with di-Ub but also with mono-Ub. However, the affinity of UCH-L3 to mono-Ub is weak compared to di-Ub (see Fig. 1B, C and Fig. 2A).

Nedd8, an Ub-like protein with 57% identity to Ub, is a previously reported UCH-L3 and UCH-L1 interacting protein (Wada et al., 1998; Hemelaar et al., 2004). Although we did not detect any derivatives of Nedd8 on LC–MS/MS analysis, Western blotting analysis of immunoaffinity-purified complexes using the anti-Nedd8 antibody revealed several bands, which presumably represent mono-Nedd8 (lower arrow in Fig. 1D) and di-Nedd8 (upper arrow in Fig. 1D).